Earth and Space Science

RESEARCH ARTICLE
10.1029/2024EA004036

Multi-Spectral Field Study of Planetary Analog Material in Extreme Environments—Alteration Products of Volcanic Deposits of Vulcano/Italy

K. Stephan[1], K. Rammelkamp[2], M. Baqué[1], S. Schröder[2], A. Pisello[3], K. Gwinner[1], G. Ortenzi[4], P. Irmisch[2], F. Sohl[1], and V. Unnithan[5]

[1]Institute of Planetary Research, DLR, Berlin, Germany, [2]Institute of Optical Sensor Systems, DLR, Berlin, Germany, [3]Department of Physics and Geology, University of Perugia, Perugia, Italy, [4]Istituto Nazionale di Geofisica e Vulcanologia, INGV, Osservatorio Etneo, Catania, Italy, [5]Department of Physics and Earth Sciences, Constructor University, Bremen, Germany

Abstract The potential of multi-spectral investigations for planetary exploration strongly depends on the specific geologic environment and related science questions. In this work, we used a visible-near infrared spectrometer, a laser-induced breakdown spectroscopy (LIBS) instrument, and a Raman spectrometer for studying acid alteration of volcanic deposits in the field as an analog for what can be potentially observed on Mars. These deposits were studied on Vulcano, one of the Aeolian Islands/Italy, where volcanic deposits are affected by active hydrothermal alteration processes and fumarolic activity. The results show that VIS-NIR spectroscopy is sufficient to identify the major minerals formed through the alteration process. This is the only technique that can identify and characterize hydrated silica, the major alteration residue, whose spectral properties vary depending on environmental conditions and the formation process. However, only LIBS spectra allow a detailed insight into the geochemistry of the pristine volcanic deposits, which is needed to define the starting point of the alteration process. LIBS also indicated the existence of chemical elements for which no corresponding mineral could be identified in the VIS-NIR data, presumably since their spectral signature is masked by strongly absorbing species. These minerals, however, could be confirmed in the Raman spectra—nicely completing the achieved results and highlighting the high potential of the sensor suite for our study.

Key Points:

- Three spectral instruments were combined to study the acid alteration of volcanic deposits as an analog for planetary exploration
- The multi-instrumental spectral investigations enabled a more complete view into the acid alteration process of volcanic rocks
- Studying the performance of each instrument in the field provides useful knowledge for future field studies and planetary missions

Correspondence to:
K. Stephan,
Katrin.Stephan@dlr.de

Citation:
Stephan, K., Rammelkamp, K., Baqué, M., Schröder, S., Pisello, A., Gwinner, K., et al. (2025). Multi-spectral field study of planetary analog material in extreme environments—alteration products of volcanic deposits of Vulcano/Italy. *Earth and Space Science*, *12*, e2024EA004036. https://doi.org/10.1029/2024EA004036

Received 21 OCT 2024
Accepted 16 APR 2025

Author Contributions:
Conceptualization: K. Stephan, M. Baqué, S. Schröder
Data curation: M. Baqué, S. Schröder, K. Gwinner, P. Irmisch
Formal analysis: K. Stephan, K. Rammelkamp, M. Baqué, S. Schröder, A. Pisello, P. Irmisch
Funding acquisition: F. Sohl, V. Unnithan
Investigation: K. Stephan, K. Rammelkamp, M. Baqué, S. Schröder, K. Gwinner, P. Irmisch
Methodology: K. Stephan, K. Rammelkamp, M. Baqué, S. Schröder
Project administration: A. Pisello, G. Ortenzi, F. Sohl, V. Unnithan
Resources: G. Ortenzi
Supervision: K. Stephan
Validation: K. Stephan, K. Rammelkamp, M. Baqué, S. Schröder, A. Pisello, K. Gwinner, G. Ortenzi

1. Introduction

The island of Vulcano enables the study of a large variety of volcanic deposits, reaching from lava flow to phreatomagmatic ash deposits and geochemical features extending from basalts to alkaline rhyolites (De Astis et al., 2013). This, together with the ongoing activity by subaerial and submarine fumaroles, provides extreme acid alteration conditions. Acidic alteration is debated to be one of the major processes at local and regional scales throughout the geologic history of Mars (Hurowitz et al., 2010; Ming et al., 2008; Nachon et al., 2014; Rapin et al., 2019; Vaniman et al., 2024) and makes this study a perfect spectral analog to constrain the types of acid alteration with regard to Mars, contributing to characterize the aqueous geochemistry in these locations and to evaluate habitable environments.

The data for this work were collected during the fifth international Vulcano Summer School (Unnithan et al., 2019) held on Vulcano in June 2019. The Summer School brought together various disciplines from planetary science, astrobiology, volcanology, geology, oceanography, engineering and robotic exploration. A wide range of instruments were utilized, such as spectrometers, underwater and terrestrial robots, a drone and hand-held devices for photogrammetry, terrain mapping, and geophysical survey equipment. In order to study the spectral properties of the volcanic deposits, we used three different spectral instruments, that is, a portable visible and near infrared spectroradiometer, a handheld laser-induced breakdown spectroscopy (LIBS) instrument, and a handheld Raman system. This combination enabled the integration of mineralogical, elemental and molecular information of the measured deposits (Rammelkamp et al., 2021, 2023; Stephan et al., 2020).

In this work, we present the spectral study of volcanic deposits based on measurements in the visible and near-infrared wavelength range and compare our results to measurements obtained by LIBS and Raman spectroscopies. Based on this field research, we discuss the potential of the multi-sensor approach to investigate volcanic deposits and their observed alteration processes. We infer possible guidelines for multi-instrument spectral analysis during future field work campaigns and planetary missions.

Visualization: K. Stephan, K. Rammelkamp, M. Baqué, S. Schröder
Writing – original draft: K. Stephan, K. Rammelkamp
Writing – review & editing: K. Stephan, K. Rammelkamp, M. Baqué, S. Schröder, A. Pisello, K. Gwinner, G. Ortenzi, P. Irmisch, F. Sohl

2. Instruments and Methods

2.1. Visible and Near-InfraRed (VIS-NIR) Spectroscopy

In the field, we used the portable spectroradiometer PSR +3,500 (spectralevolution.com), with a spectral range from 350 to 2,500 nm. Because of the numerous absorptions indicative for a wide variety of minerals, which occur in this spectral range (Hunt, 1977), such an instrument is best fit for mineralogical investigations. The instrument uses one 512-element silicon photodiode array detector with a spectral resolution of 2.8 nm up to 700 nm, and two 256-element extended InGaAs photodiode array detectors providing resolutions of 8 nm between 700 and 1,500 nm, and 6 nm between 1,500 and 2,100 nm. The measured area is 3 × 3 mm when used in situ with direct contact to the rocky surface to be studied.

In order to investigate the mineralogical assemblage, we compared the spectra measured in the field with spectral libraries containing spectra of rocks and minerals measured in the laboratory. We used a combination of several open spectral libraries containing laboratory measurements of minerals and rocks in the visible and near-infrared wavelength range, such as the USGS Spectral Library Version 7 (Kokaly et al., 2017), the PDS spectral library distributed by the PDS GeoScience Node (Murchie et al., 2007) and the MRO CRISM spectral library (Viviano-Beck et al., 2015).

For the comparison of the field and laboratory spectra, spectral matching algorithms were employed, which are implemented in the IDL/ENVI software. The used matching algorithm is a combination of two commonly used algorithms: (a) The Spectral Angle Mapper and (b) the Spectral Feature Fitting (SFF) algorithm. SAM judges how similar two spectra are based on the calculation of the angle between the spectra for each spectral band (Kruse et al., 1993). SFF uses a least-squares technique to compare a measured spectrum to a reference one (Clark et al., 1991). The comparison between the field spectra and the reference spectra with the above algorithms was done after a pre-selection through manual inspection. In order to ensure the most accurate matching result, that is, the identification of specific minerals in the field spectra, we (a) identified the most diagnostic absorptions or absorption complexes in the field spectra, (b) subdivided the field spectra into separate wavelength regions, with each wavelength region comprising the identified absorptions, and (c) applied the matching algorithm separately for each wavelength region. In this study, the most relevant absorption features are related to transition elements such as Fe^{3+} near 0.43, 0.5, and 0.9 μm and vibration absorptions of the OH, H_2O, and SO_4 groups between ∼1.3 and 2.5 μm (Cloutis et al., 2006; see Section 4).

2.2. Laser-Induced Breakdown Spectroscopy (LIBS)

For LIBS, a pulsed laser is focused onto the sample's surface, where it melts and ablates small amounts of sample material, which further evolves into a small luminous plasma. The emitted plasma light is analyzed spectroscopically for elemental analysis. For the field measurements presented here, we utilized a Sci-Aps Z-300, a commercial handheld LIBS instrument. This instrument employs a Nd:YAG laser operating at its fundamental wavelength of 1,064 nm, with a repetition rate of 10 Hz and a laser energy of 5–6 mJ per pulse. The size of the measured area on the rock surface is approximately 50 μm. Equipped with three spectrometers covering a wide spectral range of 190–950 nm with charge-coupled devices (CCD), this LIBS tool is widely employed, especially in the steel industry and increasingly in geological analysis (Connors et al., 2016; Fabre et al., 2021; Senesi et al., 2021; Wise et al., 2022). With this instrument, a constant flow of Ar gas at 12 psi can be maintained during LIBS measurements, which improves the LIBS data compared to igniting the laser-induced plasma in normal ambient conditions. Ar conditions offer stronger emission line intensities because of reduced temperature and electron density spatial gradients within the plasma plume, which minimizes self-absorption and emission line shifts (Hermann et al., 2014). However, emission lines of the atmosphere also appear in the LIBS spectra.

For our LIBS measurements, we followed the parameters described in previous studies (Rammelkamp et al., 2021, 2023), performing a 3 × 4 raster with five successive laser pulses at each point. The initial two laser pulses serve as "cleaning shots"and the plasma emission is recorded 630 ns after ignition, with an integration time of 1 ms. The measurement points of the raster are spaced by approximately 40 μm so that by accumulating all spectra of the raster, a spatial average over an area with dimensions of about ∼340 × 230 μm is obtained. In each area of interest, we performed three measurements, but in some cases, we could not use all spectra because the quality was sometimes too low for further analysis, for example, due to too large distances between laser and

sample. A detailed discussion about this challenge of measuring non-flat targets in the field with the LIBS handheld device can be found in Rammelkamp et al. (2021).

LIBS spectra initially contain qualitative information about the presence of elements in the sample. For quantitative analysis, calibration models usually have to be trained with data from known standards (El Haddad et al., 2014; Sirven et al., 2006). Since LIBS is very sensitive to experimental conditions, measurements on unknown samples must ideally be identical to measurements on the known standards. However, this is not always guaranteed, especially for field measurements with varying experimental conditions and inhomogeneous geological samples. Alternatively, statistical approaches like principal component analysis (PCA) can be used to include the entire spectrum in the analysis and to identify relative trends in a given data set. In this study, we do not provide quantitative values, but compare emission lines and also perform a PCA. The data preparation for the PCA is done as described in Rammelkamp et al. (2021), including masking the Ar emission lines introduced from the atmosphere not containing any relevant information about the samples. Emission lines are identified by comparison with databases of atomic emission lines such as NIST (Kramida et al., 2023).

2.3. Raman Spectroscopy

Raman measurements in the study area were mainly intended to be used for astrobiological research, to characterize traces of life detectable by Raman spectroscopy in the context of Mars exploration. Indeed, current and future rover missions to Mars (Perseverance, part of NASA's Mars 2020 mission, the Rosalind Franklin rover part of ESA's ExoMars mission, and the Martian Moons eXploration (MMX) mission) are carrying Raman spectrometer instruments (Beegle et al., 2015; Cho et al., 2021; Maurice et al., 2021; Rull et al., 2017; Schröder et al., 2023; Wiens et al., 2021). Raman spectroscopy is a rapid and non-destructive technique, particularly suited for identifying organic biosignatures within their geologic and mineralogical context on Earth (Böttger et al., 2013; Ellery & Wynn-Williams, 2003; Foucher et al., 2015). In the context of mineral alteration of volcanic products, Raman has been widely used to identify primary and secondary (alteration) minerals potentially missed by other techniques (e.g., Ikehata et al., 2021; Marcaida et al., 2019). In the present study, Raman measurements were used for mineral identification in conjunction with the VIS-NIR spectra and LIBS data.

The portable Raman instrument used in the field was the EnSpectr RaPort (Enhanced Spectrometry, Inc., San José, CA, United States). It has a "pistol-like" configuration with a mass around 2 kg. For excitation, the instrument has a continuous wave and frequency doubled Nd:YAG laser emitting at 532 nm. For the spectral part, a single grating spectrometer without any moving parts is part of the instrument. The EnSpectr RaPort utilizes a 30 µm entrance slit, a 1,800 g/mm holographic grating, a low pass filter, and a 30 mW single mode laser emitting at 532 nm and collecting spectra in a broad spectral range from 90 to 4,000 cm^{-1}. The size of the area measured by the EnSpectr RaPort Raman spectrometer is around 0.5×0.5 mm and, therefore, smaller than the one of the VIS-NIR spectrometer, but similar to the one of the LIBS instrument. For measurements, an automatic mode can be used in which different acquisition parameters, such as exposure times and number of accumulations, are tested and optimized. The goal is to automatically enhance the signal-to-noise ratio and to avoid saturation (fluorescence) of the detector (Němečková et al., 2020). This was the preferred mode used during field investigations. Depending on the geometry of the investigated outcrop or samples, the portable Raman instrument was either directly put in contact with the area of interest and held still during the whole measurement acquisition, or the sample itself (chipped rock) was held still covering the measurement head of the instrument.

The recorded spectra were visualized directly with the instrument's software, which possesses a built-in database recognition tool for fast identification and processing. Batch processing was further implemented with Python library RamanSpy (Georgiev et al., 2023) for spectra pre-processing (cosmic ray removal, cropping, and background subtraction), plotting, and comparison to the RRUFF online database and the corresponding publications for mineral identification (Georgiev et al., 2023; Lafuente et al., 2016).

3. Geologic Context of the Study Area

3.1. Vulcano Island and Fossa Caldera

Vulcano is part of the volcanic archipelago known as the Aeolian Islands, located northeast of Sicily (Italy) in the Tyrrhenian Sea (De Astis et al., 1997). Around 400 ka ago, the subduction of the African plate under the Eurasian plate started to trigger tectonic instability and rising of magma in this area, which resulted in volcanic activity in

10.1029/2024EA004036

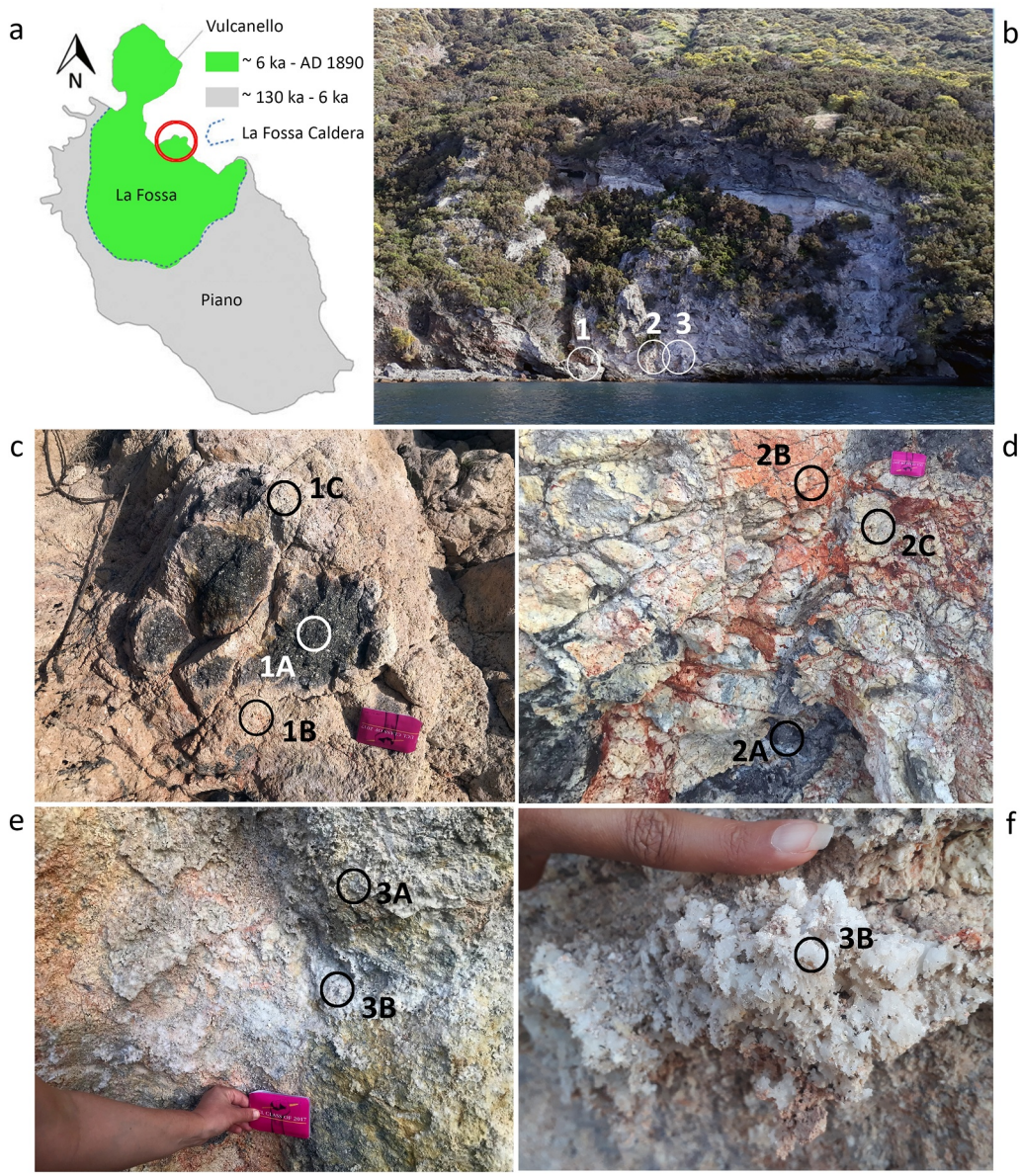

Figure 1. (a) Simplified geologic map of Vulcano (adapted from Dallara et al., 2023) with the location of the study area indicated by a red circle; (b) the study area at the foot of the La Fossa caldera as seen from the sea side, and with investigated spots 1–3 indicated by the white circles; and a close up look onto the spectrally investigated points in panel (c) spot 1, (d) spot 2, and (e) spot 3; (f) close up view onto white crystals in point 3B. The spectrally measured points discussed in Section 4 are indicated by circles and letters.

the region (Peccerillo, 2005). The deposits on the island consist of volcanic products resulting from various processes: we can find lava deposits from effusive emplacement of magma, as well as extensive ash deposits from different phases of explosive volcanic activity on the island. Moreover, condensed sulfur deposits on the lava rocks originating from the numerous active fumaroles on the island are also present.

The oldest parts of Vulcano have been dated at 130 ka, while the last eruption occurred in the 1890s (Dallara et al., 2023; Figure 1a). Due to the NW migration of vents, the volcanic activity gave first birth to a large stratocone occupying the southern part of the island (Piano caldera, ∼130–6 ka), followed by the La Fossa caldera, whose subaerial formation started at about 6 ka (Dallara et al., 2023; De Astis et al., 2013). The youngest volcanic edifice on the island is represented by the Vulcanello peninsula (AD 900–1,600; Arrighi et al., 2006; Dallara et al., 2023; Di Traglia et al., 2013; Fusillo et al., 2015; Malaguti et al., 2022).

The largest volcanic edifice formed by the still active volcanic centers of the island is the La Fossa volcano (Dallara et al., 2023) (Figure 1a). Pyroclastic materials and lava flow units were emplaced during three major volcanic phases. These deposits also include the Punte Nere units formed on the northern flank of the La Fossa cone (Fulignati et al., 1998), which consist mainly of lava flows erupted between 5.3 ka (Voltaggio et al., 1995) and 3.88 ka (De Astis et al., 2013; Tranne et al., 2002). Since its last eruption, numerous fumaroles fed by hydrothermal and magmatic fluids (Aiuppa et al., 2022; Mandarano et al., 2016) were particularly intense in the 1920s and have been active from 1978 to the present (Barberi et al., 1991; Dallara et al., 2023). Today, the fumarolic activity dominates the north side of the La Fossa crater and in the Baia di Levante zone at the base of the crater (Fulignati et al., 2002).

The chemical composition of the Vulcano deposits generally reflects its geodynamic setting (Dallara et al., 2023; De Astis et al., 2000, 2013). Within the last 1 million years, volcanism in the Aeolian Arc has followed an evolution toward high-K calc-alkaline rocks (De Astis et al., 2013). A wide variety of compositions ranging from basalts to rhyolites was erupted (Dallara et al., 2023; De Astis et al., 1997, 2013; Nicotra et al., 2018). The Punte Nere formation is characterized by a latitic to trachytic composition (De Astis et al., 2013) with an intermediate content of silica (58–69 wt.%), more than 4 wt.% K_2O, and a total alkaline content larger than 6 wt.% (Le Maitre, 2002). In addition, major and trace element compositions include high but variable content of Al_2O_3, CaO and MgO, low iron enrichment, and low TiO_2 but with an enrichment in other trace elements such as Ba and Sr.

3.2. Study Area in the Baia Di Levante Area

The particular scientific interest of this study is the alteration of the volcanic rocks by the fumarolic activity of the La Fossa volcano. Our case study deposits are best represented by an outcrop at the base of the steep northern flank of the La Fossa caldera (Figures 1a and 1b; De Astis et al., 2013; Di Traglia et al., 2013; Malaguti et al., 2022) directly located at the coastline in the Baia di Levante area (38°24'44"N/14.57'49"E). The horizontal and vertical extension of the outcrop reaches several tens of meters. An extensive mass of heavily altered volcanic deposits located directly below a several meters thick layer of younger lava rocks can be observed. All these rocks have been assigned to the Punte Nere formation of the La Fossa system (De Astis et al., 2006), which is dominated by trachytic 'a'ā lava flows. The formation of the sea-facing cliff hosting this outcrop was strongly aided by rock falls. Obviously, the outcrop itself has been formed by a recent collapse due to slope instability, resulting in the extensive fracturing of the rock body and the subsequent weathering of the products in the course of fluid circulation within the fractures. Thus, it can be expected that the lava rocks exposed in the outcrop were mainly altered by volcanic activity without a pronounced interaction with Earth's atmosphere so far. Nevertheless, the lava rocks are still influenced by subaerial and submarine fumarolic activity, with volcanic sulfur-rich gases emanating through cracks and caves in the mass of rocks pervading and actively altering these deposits. Therefore, this site represents a unique geologic and mineralogic analog for studying secondary mineral assemblages formed through acid and hydrothermal alteration of volcanic rocks for planetary applications such as the mineralogical investigation of the past volcanic activity and alteration processes on Mars.

Three spots were chosen for detailed spectral measurements using the three different instruments. These spots show different phases of altered lava rock, starting from less strongly altered lava rocks to pervasively altered portions (Figure 1b). Depending on existing surface color variations, different points were defined for each spot and separately spectrally investigated. A large block of strongly altered massive trachytic lava, presenting a heavily altered rim and an only weakly altered core, was chosen as spot 1 (Figure 1c) to study the various degrees of alteration processes from the inner, relatively fresh, lava rock toward the outer, completely altered portions. The less strongly altered inner part of the rock (unit 1A) is characterized by the preservation of a gray microcrystalline groundmass, but with the numerous pores typically present in the fresh lava already filled with mineral deposits that dominate also the remaining portion of the rock's surface. Red (unit 1BI) to pink (unit 1BII) and yellow to white portions (unit 1C) are visible. Spot 2 (Figure 1d) is dominated by a highly fractured portion of already strongly altered lava rocks showing dark gray, presumably more pristine (unit 2A), and more altered parts with surface colors ranging from red (unit 2B) to yellow and white (unit 2C). Spot 3 (Figure 1e) is characterized by a rather solid block of highly altered lava rock with only small color variations and a rather gray (unit 3A) and white crust (unit 3B) with particular crystal growth (Figure 1f).

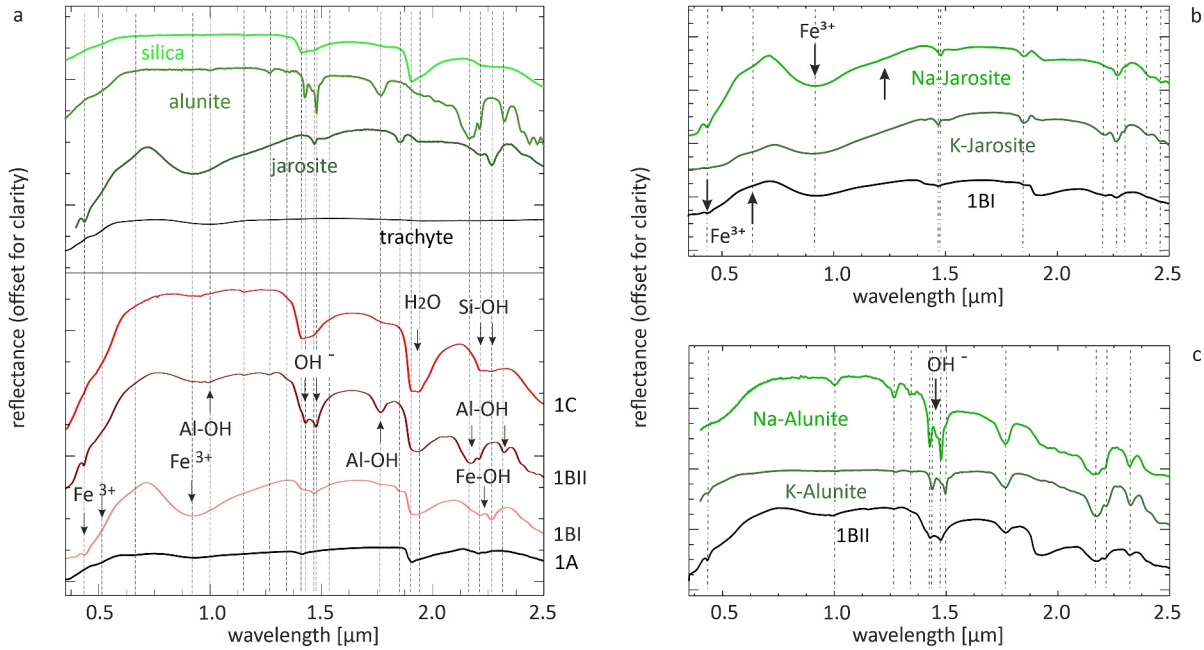

Figure 2. VIS-NIR field spectra (shown in reddish colors) taken at (a) spot 1 compared with reference spectra (greenish colors, from USGS, PDS and MRO CRISM spectral library) that show the best spectral fitting to the field spectra and (b) point 1B of spot 1 compared with reference spectra of K- and Na-rich jarosite and alunite (CRISM spectral library). The IDs of the reference spectra are: BKR1JB329C (silica), GDS24 Na and JR2501K (jarosite), AL706 Na and GDS84 Na03 (alunite), c2an21a (trachyte). The positions of the diagnostic absorptions are indicated.

4. Spectral Variability Indicated by VIS-NIR Results

4.1. Spot 1

Figure 2 presents the VIS-NIR spectra taken at spot 1 compared with laboratory spectra of minerals exhibiting similar spectral characteristics. Spectra taken at spot 1 show the largest variety of spectral signatures and corresponding mineralogy detected in the study area. Spectra of the most unaltered dark and gray parts in point 1A (Figure 2a, spectrum 1A) show a positive visible spectral slope until 0.7 µm (with a slight depression at 0.5 µm) and a rather flat spectral continuum up to 2.5 µm. Only a broad, shallow Fe-related absorption at 0.9 µm and weak absorptions at 1.4, 1.9, and 2.2 µm are recognizable (Figure 2a, spectrum 1A). The spectral properties of these lava rocks are best represented by laboratory spectra of trachyte (Figure 2a). The shape of the spectrum is also comparable to the shape of amorphous shoshonitic/trachytic silicate glasses (Pisello et al., 2022), which present a positive slope until about 0.8 µm and a flatter aspect at higher wavelengths. The additional absorptions already indicate some degree of alteration. The absorptions at 1.4 and 1.9 µm occur in minerals with hydroxyl groups (OH^-) or water (H_2O), respectively. The absorption at 2.2 µm indicates Al rather than Fe/Mg bearing silicates with Al-OH and Si-OH bonds (Ehlmann et al., 2009).

The adjacent areas in spot 1, that is, point 1B (Figure 1c), are characterized by a strongly altered red to pinkish surface. The associated spectra show numerous additional absorptions (Figure 2a, spectra 1BI and 1BII) characteristic for sulfates (Hunt et al., 1971). The absorptions can be related to the presence of transition elements, OH, H_2O, and SO_4 groups (Bishop & Murad, 2005; Cloutis et al., 2006). Absorption bands located at 0.43, 0.91, 1.47, 1.85, and 2.27 µm (Figure 2a, spectrum 1BI) are diagnostic for Fe-rich jarosite (K, Na $Fe_3(SO_4)_2(OH)_6$). Absorptions located at 1.76 and 2.17 µm (Figure 2a, spectrum 1BII) indicate the presence of Al-bearing alunite (K, Na $Al_3(SO_4)_2(OH)$). The reddish color of the rock's surface could be related to the relative strong Fe^{3+} absorption near 0.9 µm in the spectrum of jarosite (Figure 2a, spectrum 1BI), whereas less red, rather pinkish surface areas could be associated to the dominance of alunite, with the Fe^{3+} absorption almost not visible anymore (Figure 2a, spectra 1BII).

Even more, the spectral resolution of the field spectra allows distinguishing different cations incorporated in jarosite and alunite. In comparison with reference spectra, it appears that both K^+ and Na^+-enriched versions of

10.1029/2024EA004036

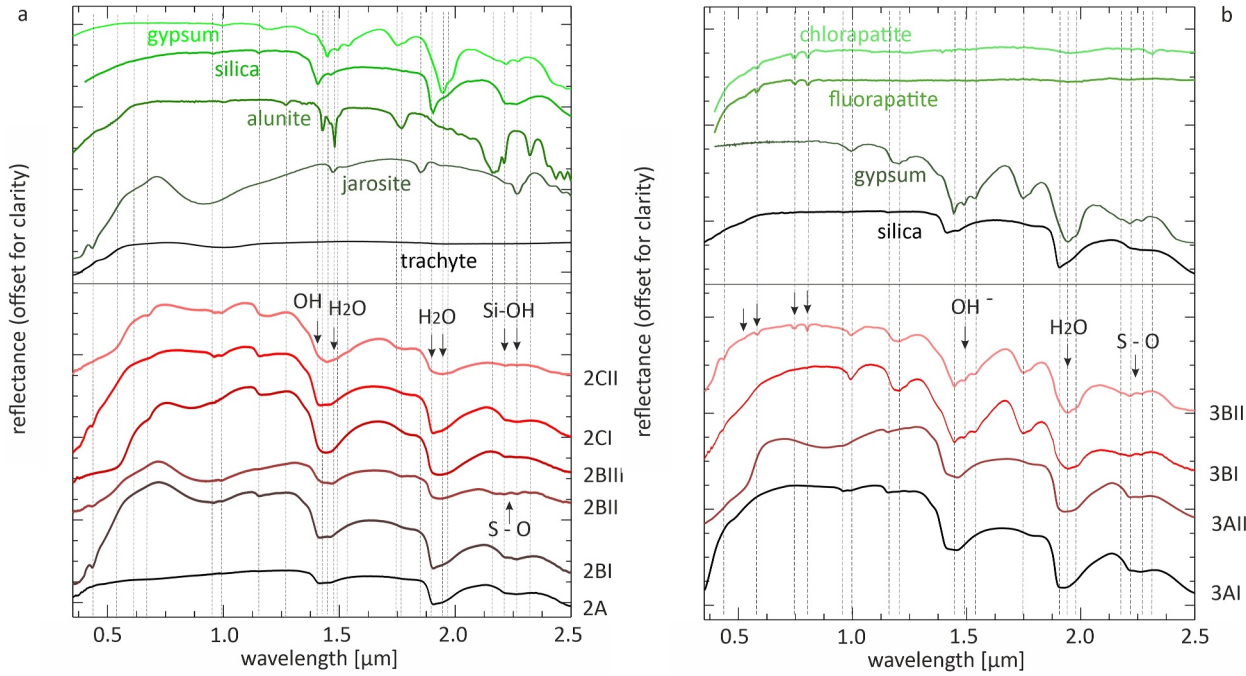

Figure 3. VIS-NIR field spectra (shown in reddish color scale) taken at (a) spot 2 and (b) spot 3 compared with laboratory spectra (greenish color scale, from PDS and MRO CRISM spectral library) that show the spectra of identified minerals in spot 1 and additional best spectral fitting to the field spectra. The IDs of the spectra are: CASF41 (gypsum), WS416 and WS423 (F and Cl apatite) and as stated for Figure 2. The positions of the diagnostic absorptions are indicated.

these minerals could exist in point 1B (I and II) (Figures 2b and 2c) either as a spectral mixture of their spectral signatures or one of them dominating the individual absorption features in the field spectra. The OH- bands near 1.4 µm occur at longer wavelengths in Na-bearing jarosite (1.47–1.48 and 1.541–1.546 µm) than in K-bearing jarosite (1.465–1.468 µm and 1.51–1.52 µm) (Figure 2b and Cloutis et al., 2006). Furthermore, the OH combination bands in the 1.8 µm region occur at longer wavelengths in Na-bearing jarosite (1.85–1.86 µm) than in K-bearing jarosite (1.84–1.85 µm). Differences are also seen in the wavelength positions of the S-O fundamental bands.

The spectrum acquired in point 1C, which exhibits a rather yellow rock surface, shows an asymmetric OH^- absorption centered at 1.41 µm and a complex H_2O absorption with two minima at 1.91 and 1.96 µm (Figure 2a, spectrum 1C). At 2.21 and 2.26 µm, however, the Si-OH absorption complex can be identified. These absorptions are best fit by reference spectra of siliceous sinter (Rice et al., 2013), a specific type of group of materials named "hydrated" silica. The term is used for minerals that are comprised almost entirely of SiO_2 x nH_2O (<0.5 mol% non-volatile impurities; Graetsch, 1994). Water (H_2O) and/or hydroxyl (OH) can be either bound in the molecule structure or adsorbed on the surface (Flörke et al., 1991).

4.2. Spot 2

Although the rocky surface in spot 2 also exhibits the same diverse coloration as seen in spot 1, with the appearance of the surface in the different points (Figure 1d, and 2A–2C) changing from gray to red and yellow, respectively, the VIS-NIR spectra of the area (Figure 3a, spectra 2A–2C) appear more uniform. In comparison with the spectra of materials identified in spot 1, the acquired spectra in spot 2 do not show any strong indication of unaltered lava rock and/or sulfate minerals alunite and jarosite. Instead, the spectral signature of all spectra seems to be dominated by hydrated silica with a weak absorption at 0.95 µm, the asymmetric hydroxyl (OH^-) and/or water (H_2O) bands near 1.4 and 1.9 µm, respectively, as well as the Si-OH absorptions at 2.21 and 2.26 µm.

In general, the absorptions of the hydrated silica in spot 2 correspond to the ones measured in spot 1. However, in contrast to spot 1, the wavelength position of the absorption at 1.4 µm varies more strongly throughout the measured points in spot 2 and shifts from an asymmetric absorption at 1.41 µm (spectra 2A, 2BI and 2CI) to a more symmetric absorption at longer wavelengths or shows additional absorptions at longer wavelengths

(1.44 μm, spectra 2BII, 2BIII and 2CII). The same trend can be observed for the absorption near 1.9 μm; whereas, spectra 2A, 2BI, and 2CI show an asymmetric absorption at 1.91 μm, the minimum of the absorption shifts to 1.94 μm in spectra 2BII - III and 2CII shifts to 1.94 μm.

These changes possibly indicate a higher degree of silica hydration. However, spectral differences are also apparent in the visible spectral range up to 1.3 μm. Particularly, spectra 2BI to II show a prominent Fe^{3+} absorption near 0.9 μm that corresponds to the reddish surface of point 2B (Figure 1d). In addition, spectrum 2BII shows several additional absorptions in the 2.2 μm-area that also occur in gypsum. The tiny absorption at 0.43, ∼0.9, and 1.85 μm recognizable in the spectra 2BI–III and 2CI–II, also occur in the spectra of jarosite and alunite. Thus, the observed small changes in the absorptions dominated by hydrated silica could also be caused by small amounts of gypsum, jarosite and alunite.

4.3. Spot 3

In spot 3, the spectra taken in the gray areas of point 3A (Figure 3b, spectra 3AI and II) also show the spectral signature of hydrated silica with the spectral characteristics corresponding to silica sinter (Rice et al., 2013). The spectra of the whitish surface areas in point 3B (Figures 1e and 1f, spectra 3BI and II in Figure 3b), however, show absorptions characteristic for gypsum ($CaSO_4 \times 2H_2O$) as the main species with its prominent H_2O- and S-O-related complex absorptions at 1.4, 1.75, 1.9 μm as well as at 2.17, 2.22, and 2.28 μm (Anbalagan et al., 2008). Again, the tiny absorption at 0.43 μm in the spectra 3BI and 3BII could also be related to minor amounts of jarosite in this area (Figure 3b).

Intriguingly, in the visible portion of the spectra dominated by gypsum (Figure 3b, spectra 3BI and II), several weak and narrow absorptions appear that cannot be associated with gypsum. The absorptions are located at 0.53, 0.58, 0.68, 0.74, and 0.80 μm and could only be found in spectra of apatite ($Ca_5(PO_4)_3(OH,F,Cl)$). In Figure 3b, the spectra taken in the field are compared to the ones of chlor- and fluorapatite. Both varieties show these absorptions, making it difficult to determine which variety causes the spectral signature in the field spectra.

5. Comparison of the VIS-NIR With LIBS and Raman Measurements

5.1. LIBS Results

Figure 4 shows zooms to selected ranges of the LIBS spectra acquired in spot 1 (Figure 1c) averaged per defined point (1A, 1B, 1C). In general, LIBS data confirm the presence of most of the chemical elements expected for volcanic lava rocks in the study area, which include: Si, Fe, Na, K, Ca, Al, Ti, S, Sr and Ba. Although, in this study, no quantitative values are given for the abundances of the respective elements based on the LIBS spectra, the relative line intensities still indicate variations in the relative element abundance between the measured points in spot 1 (1A, 1B and 1C) and are therefore sufficient to use for supporting the interpretation of the VIS-NIR spectra.

The Fe (II) emission lines around 275 nm (Figure 4a) are relatively weak in point 1A. In point 1B, these lines vary from relatively strong in portions of the rock's surface that appear dark red (1BI) to relatively weak in regions that appear light red to pinkish (1BII). Apparently, this observation is consistent with the existence of Fe-rich sulfate jarosite together with non-Fe-bearing alunite in point 1B as identified in the corresponding VIS-NIR data (Figure 2a, spectra 1BI and 1BII, respectively). Moreover, the S atomic emission S (I) at 921.4 nm (Figure 4i) appears in the spectrum of point 1BI in line with the presence of jarosite. The S (I) line is even stronger in 1BII, which will be further discussed below. S could be only tentatively seen in the corresponding LIBS spectra of point 1C, where hydrated silica could be identified in the VIS-NIR (Figure 2a, spectrum 1C). In addition, LIBS data do not show a clear trend regarding the Al (I) emissions at 396.13 and 394.38 nm (Figure 4d), which could have supported the distribution of alunite in spot 1. Si is present, as identified at 288.14 nm (Figure 4c), everywhere, but apparently is less prominent in point 1B, where the sulfates jarosite and alunite were identified in the VIS-NIR data (Figure 2a, spectra 1BI and 1BII). In comparison, Si is most prominent in points 1A and 1C, that is, in the more or less unaltered portion and, where hydrated silica dominates the spectral signature in the VIS-NIR (Figure 2a, spectra 1A and 1C). LIBS data also identify Ca in spot 1 (Figures 4d and 4e), with the strongest Ca lines in point 1A and less strong in points 1B and 1C. Possibly, Ca detected by LIBS belongs to the more or less unaltered lava rock, which, during the alteration process, is consumed by the formation of gypsum as identified in the VIS-NIR spectra in spot 2 and especially spot 3. LIBS data also nicely show the presence of Sr (Figure 4e)

10.1029/2024EA004036

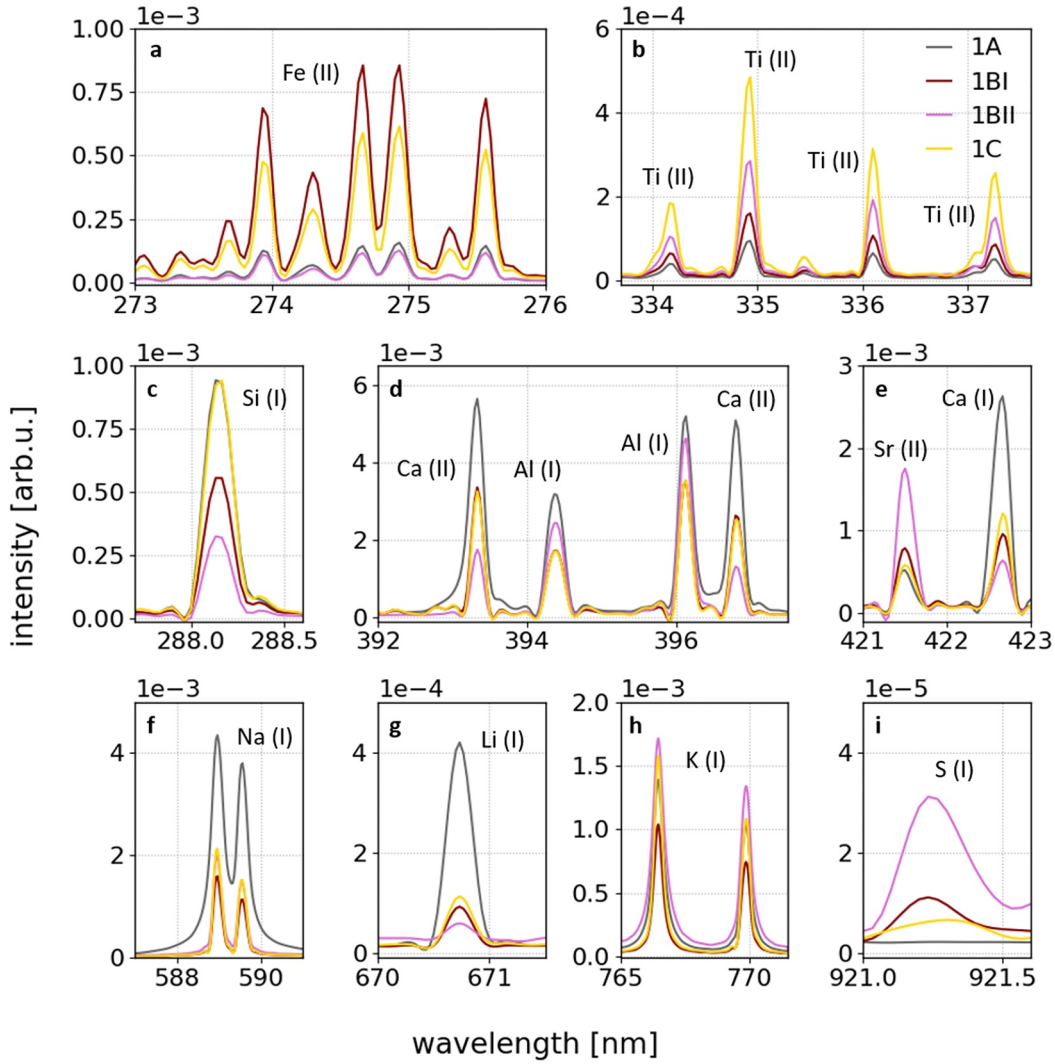

Figure 4. Zooms on spectral regions showing the laser-induced breakdown spectroscopy emission lines of selected elements. Average spectra are shown for each point (1A–1C) at spot 1, normalized to their total intensities.

which is particularly strong in the spectrum from 1BII. Since also S is present in this point, LIBS data support the existence of Sr-bearing sulfates in the study area. Finally, Ti is present in all points of spot 1 (Figure 4b) with an increasing emission line strength from point 1A to 1C, which supports the existence of a Ti-bearing mineral, especially for point 1C. Thus, LIBS data possibly indicate additional minerals that could not be detected in the VIS-NIR data.

As noted in the literature (De Astis et al., 2013), lava rocks often contain Na and K, which is also the case for the rocks measured at spot 1, as confirmed by emission lines in the LIBS spectra (Figures 4f and 4h). The alkali metals behave differently in the different locations. For Na, it can be seen that it is significantly stronger in the unweathered lava rock (unit 1A) compared to the other points (Figure 4f). K, on the other hand, is similarly strong in the altered portions of the rock (units 1B and C) as in the original lava rock (unit 1A). Still, small differences in K emission line strength can be seen—it is strongest in 1BII and weakest in 1BI, with sites points 1A and 1C in between. This could support the findings derived from the VIS-NIR that jarosite and alunite occur in both varieties, that is, in their K- and Na-rich versions in point 1B (Figures 2b and 2c, spectra 1BI and 1BII), respectively.

For further analysis of the LIBS data, including the spectra from spots 2 and 3, a PCA as described in Rammelkamp et al. (2021) was performed. A total of 28 spectra from all three spots were included, and with 6 principal components (PC) more than 95% of the variance in the data set could be explained. Here we focus on the

10.1029/2024EA004036

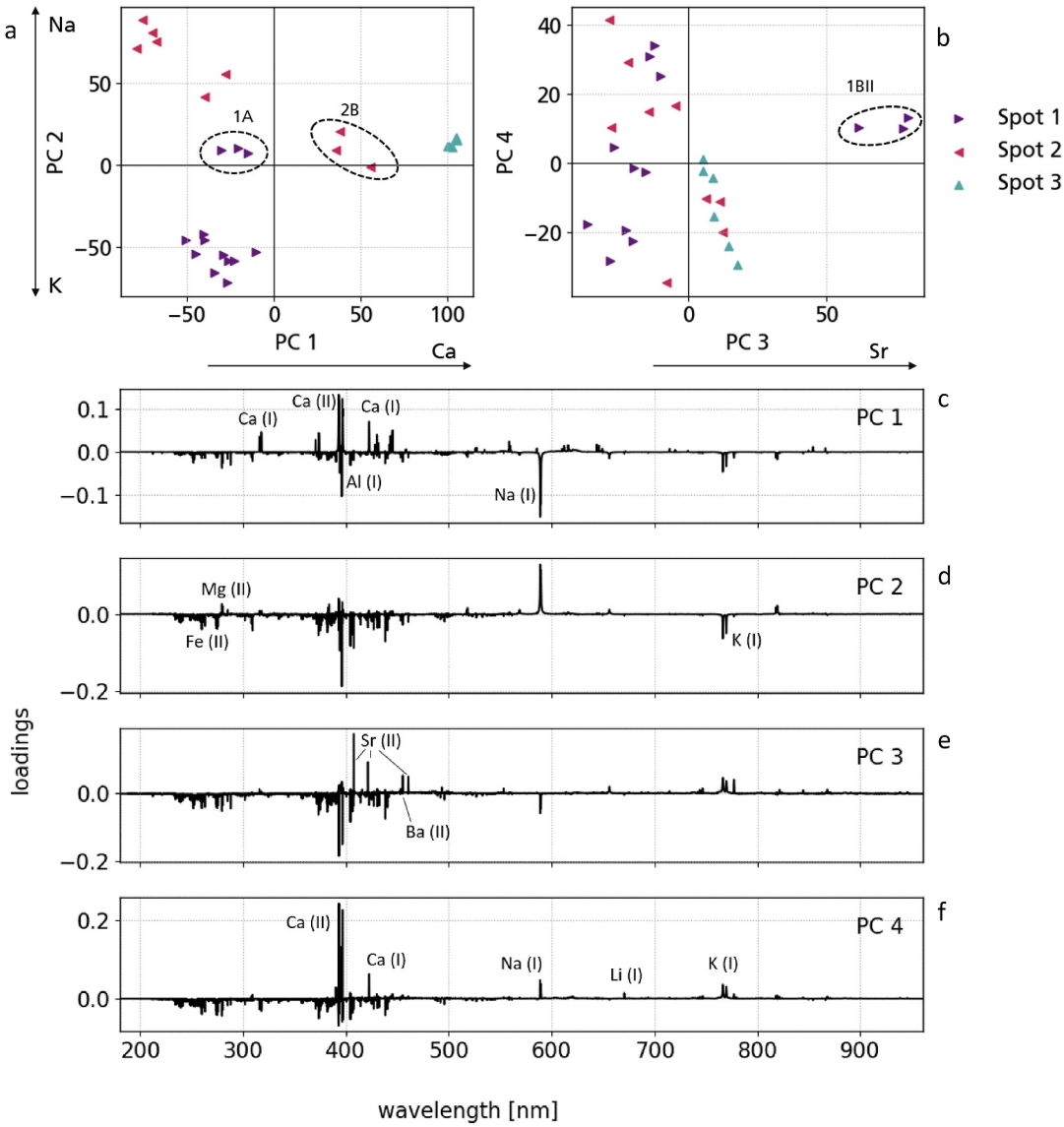

Figure 5. Principal component analysis scores with respect to (a) principal components (PC) 1 and 2 and (b) PC 3 and 4 of all laser-induced breakdown spectroscopy spectra measured at spot 1 to 3. The assignments of elements to the PCs is based on the loadings of (c) PC1, (d) PC2, (e) PC3 and (f) PC4. For clarity, annotations of the elements are not shown for every PC.

first 4 components, as they cover all the observations relevant for this study. The scores are shown as scatter plots in Figures 5a and 5b. The loadings can be seen in Figures 5c–5f. The latter show pixel-wise (wavelength-wise) positive and negative correlations, which often correspond to emission lines and can therefore support interpretations of relative elemental abundances (Abdel-Harith et al., 2022). The higher or lower the score value of a spectrum on a PC, the better the spectrum is described by that PC. For example, all spectra measured at spot 3 have high positive scores on PC 1 (see Figure 5a), and the loadings of PC 1 are positively correlated with mostly Ca emission lines (see Figure 5c). This means that spot 3 spectra have stronger Ca emissions and therefore probably more Ca abundance than the other spots. This is in line with the VIS-NIR spectra measured at spot 3 (Figure 3b), which are dominated by the presence of Ca-bearing minerals, mainly gypsum. Looking at the PC 1/PC 2 plot (Figure 5a), three clusters can be seen according to the measurement site, except for a few scores of spot 1 and 2 spectra. As described above, the spot 3 cluster is characterized by strong Ca emission according to the loadings of PC 1 (Figure 5c). In addition to spot 3 spectra, the spectra measured in point 2B at spot 2 also have positive scores on PC 1, but to a lesser extent than spot 3 spectra, indicating somewhat higher Ca at this point in comparison to other points of spot 1 and spot 2.

This observation is compatible with the occurrence of some gypsum also at spot 2 (Figure 3a, spectrum 2BII). Spot 1 and 2 can be distinguished based on PC 2, whose loadings indicate a positive correlation with Na and a negative one with K emission lines (Figure 5d). This means that spot 2, whose spectra have mostly positive PC 2 scores, is enriched in Na compared to spot 1, whose spectra have mostly negative PC 2 scores, indicating more abundant K. The only spectra of spot 1 with positive scores on PC 2 are from the gray area (unit 1A). In the PC 3/PC 4 plot (Figure 5b), the spectra measured in point 1B at spot 1 with more pinkish material (Figure 2a, spectrum 1BII) stand out with positive scores on PC 3. This is in line with the observation from the emission lines discussed above (also see Figure 4), as this point shows strong Sr emission lines, and those lines also dominate the loadings of PC 3 (Figure 5e). Interestingly, Ba emission lines have a positive correlation with PC 3, too, indicating that in addition to Sr, there is also a higher Ba concentration in the pinkish-colored portion of point 1B (1BII) at spot 1 than in other points, supporting the existence of Sr as well as Ba-bearing minerals that could complement the VIS-NIR results.

Another mineral that was identified in the VIS-NIR spectra is apatite in spot 3 (Figure 3b, spectrum 3BII), in which the LIBS spectra are dominated by Ca emission lines. Although Ca is part of apatite, we could not observe other elements indicative of apatite such as P, Cl, or F in the LIBS spectra. As mentioned above, limits of detection with LIBS are element dependent. In particular, halogen elements such as Cl and F can be challenging to observe. If Ca is present in the point as well, as it would be the case for apatite, those elements can temporarily form the simple molecules CaF and CaCl in the LIBS plasma which would be observable in the spectrum as broad molecular bands (Vogt et al., 2020). However, neither elemental emission lines nor molecular bands were observed in the spectra. This is not in contradiction with the VNIR observations, as it is possible that the small apatite crystals were not targeted with LIBS.

5.2. Raman Results

Raman measurements nicely confirmed and/or complemented the VIS-NIR results in conjunction with the LIBS data. For comparison, selected field spectra are shown together with spectra from the RRUFF reference database (Figure 6), and the results are checked based on previously published studies. Alteration minerals such as jarosite and alunite could be identified in spots 1 and 2 (Figures 6a and 6b), thus confirming their identification based on VIS-NIR spectra (Figures 2a and 2b). Numerous Raman features could be observed that can be used to distinguish these minerals (Liu et al., 2020) and are mainly assigned to SO_4^{2-} and OH^- vibrational modes presented in previous studies (Frost et al., 2005, 2006). The influence of Fe or Al in spectra of alunite and jarosite, respectively, was studied by Murphy et al. (2009) and showed major differences in the vibration band positions of the sulfate group and Al-O or Fe-O bonds. In the acquired spectra, mostly both jarosite and alunite are detectable (Figure 6b). Only a few spectra are dominated by the spectral signature of alunite. Since the band position of the vibrational modes concerning the sulfate- and hydroxyl groups is also dependent on the ionic radius of the monovalent cations K+ and Na+ (Ling et al., 2015; Maubec et al., 2012), it is possible to distinguish K- and Na-rich alunite as seen in the VIS-NIR spectra. Although Raman spectra suggest that both K- and Na-rich alunite could be present, the absence of a peak around 465 cm^{-1} suggests Na-rich alunite in point 1B at spot 1 (Figure 6a).

Although no spectral features could be detected in areas dominated by hydrated silica, as indicated by the VIS-NIR spectra, Raman features associated with sulfates such as gypsum ($CaSO_4 \times 2H_2O$; Liu et al., 2009) are clearly visible at spot 3 (spectrum measured in point 3A, Figure 6c) based on the major Raman mode slightly below 1,000 cm^{-1} but also on weaker modes around 450, 630, and 1,100 cm^{-1}. However, other sulfates, such as barite ($BaSO_4$) and celestite ($SrSO_4$; exhibit Raman features at similar wavelengths and thus could exist in the study area (Chen et al., 2010; Mabrouk et al., 2013). In addition to the sulfate Raman modes, sulfur modes can also be seen in a spectrum taken in point 3A at spot 3 (Figure 6c). Additional spectra measured in point 3B of spot 3 can be assigned to celestite (spectrum 3BI, Figure 6d), the presence of which was already suspected from the LIBS data. Intriguingly, Ti-bearing minerals such as anatase (TiO_2; Murad, 1997; Hope et al., 2001; Edwards et al., 2006) suggested by the LIBS data, could be also identified in some Raman spectra derived from areas dominated by gypsum (spectrum 3BII, Figure 6e). Apparently, these minerals exist close to each other and within the area of point 3B as defined by the VIS-NIR measurements. Although VIS-NIR spectra show no indication of either barite, anatase, and celestite, Raman data support the existence of these minerals in the study area. In contrast, similar to the findings based on LIBS data, Raman data show no spectral features that could be associated with phosphates such as apatite (Zhukova et al., 2022) and therefore could not confirm the indication of the apatite by the VIS-NIR spectra (see Section 4.3).

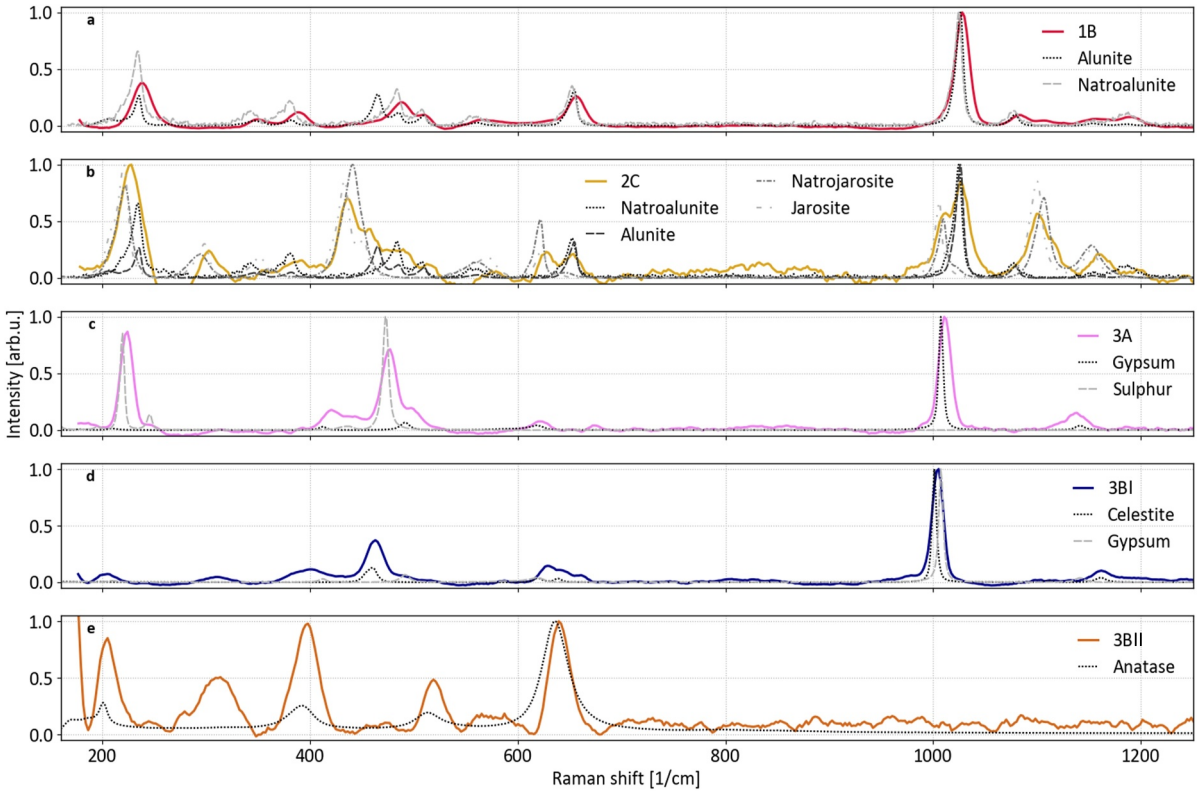

Figure 6. Raman spectra acquired in the field at the points in panel (a) spot 1, (b) spot 2 and (c–f) spot 3 compared with reference spectra from the RUFF spectral library (https://rruff.info/). The IDs for the spectra are: R060430 (Alunite); R060406 (Natroalunite); R060113 (Jarosite); R050289 (Natrojarosite); R040029 (Gypsum); Celestite (R040007); Anatase (R120013) The feature between 200 and 400 cm^{-1} in panel (e) is likely an artifact from the baseline subtraction. All Raman spectra were smoothed with an moving average with a window size of 5. See the text for explanation of the specific Raman features.

6. Discussion—Alteration Processes in the Baia di Levante Area as Analog for Mars

Multi-instrumental spectral investigations enabled to achieve a more complete view of the mineralogical composition of the study area, which is needed to gain more insight into what we can learn from the combined spectroscopic analyses about the acid alteration process of volcanic rocks. An overview of the results with all three techniques can be found in Table 1, in which the identified minerals/rocks with VIS-NIR and Raman spectroscopy are listed, as well as the qualitatively most dominant elements identified with LIBS. For most

Table 1
Overview of Mineral Identification Synergies With All Three Techniques per Spot and Point

Spot	Unit	Subunit	VIS/NIR	LIBS	Raman
1	A	I	Trachyte	**Na, Li, Si,** Ca, K	Pyroxene
	B		Jarosite	**Fe,** S	Jarosite
		II	Alunite	**Sr,** Ba, **K,** S	Alunite, gypsum
	C		Hydrated silica	**Si,** K	–
2	A		Hydrated silica	**Si, Na,** Fe, S	–
	B		Hydrated silica gypsum (?)	**Na**, Ca	–
	C		Hydrated silica	**Ca,** Fe, S	Alunite/jarosite
3	A		Hydrated silica	**Ca, Sr**, S	Gypsum, sulfur
	B		Gypsum, apatite	Strongest **Ca**, S	Gypsum, celestite, anatase, sulfur

Note. In some points no Raman features could be identified. For LIBS, only the elements with dominant emission lines are given which is a relative assessment based on the PCA (Figure 5). Elements in bold indicate particular strong emission lines.

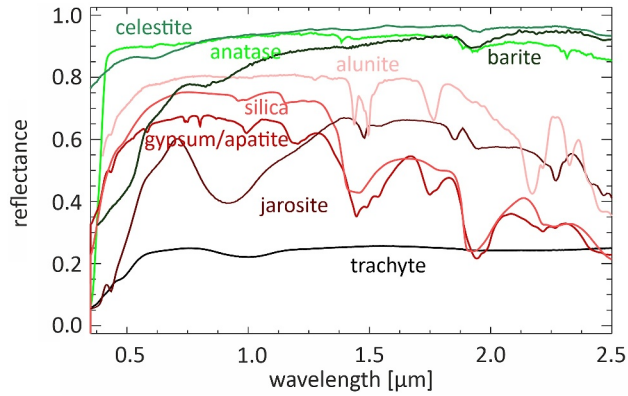

Figure 7. Reference spectra of minerals (from PDS and MRO CRISM spectral library) detected in spots 1 to 3 compared to minerals containing Sr, Ti and Ba such as the sulfates celestite, anatase and barite. IDs of the spectra are: HS79.3B (barite), 397s213w (anatase), c1jb639a (celestite).

elements that LIBS detected in the study area, corresponding alteration minerals could be detected in the Raman and/or in the VIS-NIR spectra. Even more, only LIBS data provided essential knowledge about the elemental composition of the pristine lava rocks. Without this information, no direct evidence can be named for the starting point of the alteration path of the lava rocks on Vulcano. Therefore, LIBS or any instrument solving the elemental composition of the target rock is essential for studying and characterizing lava rocks on terrestrial bodies.

VIS-NIR and Raman spectroscopy are powerful tools for the detection, discrimination and characterization of alteration and hydrothermally formed minerals due to the availability and diversity of numerous spectral features related to OH^- and H_2O in these wavelength regions (Cloutis et al., 2006). Furthermore, slight differences in the spectral signature could even be used to distinguish compositional differences within a mineral family (Na- or K-rich alunite or jarosite). VIS-NIR and Raman techniques nicely complement each other in case of their transparency or activity in the associated spectra range, as seen in the case of anatase and celestite.

The combination of the three instruments, however, enabled to identify additional sulfates incorporating trace elements (Ba, Sr) such as celestite and barite, as well as Ti-bearing anatase. These minerals could not be detected in the VIS-NIR spectra. The reference spectrum of celestite is quite bland and transparent compared with the VIS-NIR spectra of identified minerals in the study area (Figure 7). The same accounts for the reference spectrum of anatase. Beside a different spectral slope in the visible spectral range, barite also lacks characteristic spectral features in the near-infrared wavelength range. Therefore, it cannot be excluded that these minerals exist in the study area, but with their spectral signatures potentially superimposed and masked by the spectral signatures of the other detected minerals.

Celestite is well known to occur in evaporitic sediments and in association with gypsum ($CaSO_4 \times 2H_2O$) or anhydrite ($CaSO_4$) (Qiu et al., 2019) and is suggested to form through the replacement of Ca by Sr (Forjanes et al., 2020). Anatase is a mineral that occurs in a large variety of geological settings. Hot, mineral-rich fluids circulating in the crust can lead to the formation of anatase. These fluids may dissolve titanium from surrounding rocks and then deposit anatase as they cool. Both minerals are hydrothermally formed accessory minerals, which apparently are associated with gypsum. The same could account for apatite caused by acid gases HCl and HF (Bolognesi & D'Amore, 1993; Chiodini et al., 1995; Capasso et al., 1997; Gioncada et al., 1998; Dallara et al., 2023). Apatite's presence is indicated by the VIS-NIR spectra; however, its existence could not be confirmed neither by LIBS nor by Raman measurements. Nevertheless, apatite is known as a widespread trace mineral in most igneous rocks (Belousova et al., 2002), mostly occurring as small crystals in the groundmass in volcanic rocks or hydrothermal deposits. Even more, apatite has been identified as a common accessory mineral in shoshonitic volcanic deposit of the La Fossa volcano (Dallara et al., 2023).

The combined use of three different spectral field instruments showed that special care has to be taken to align the measurement locations of the different spectral instruments due to the different field of view (FOV) of the instruments. Ideally, we would want to scan the same area with all spectral instruments sequentially or with adapting the spot sizes. However, potential alteration effects by LIBS measurements need to be considered when planning the sequence of measurements (Schröder et al., 2020). The accurate determination of the location of the LIBS and Raman measurements within the VNIR spot area is absolutely necessary. Contrary to instruments on rovers for planetary missions, where the alignment and geometric properties of the different instruments are well known, in the field it is more challenging to measure the same portion of the surface by subsequent measurements of the different handheld instruments. In the case of apatite, the identification could be even more difficult due to the different sizes of measurement areas covered by the instruments (Section 2) combined with the apparently small size of individual crystals of apatite in the gypsum-dominated area. This possibly could account for the partly non-identification of any existing apatite in the study area.

The observed abundant hydrated silica could be characterized in detail only based on the VIS-NIR spectra. Therefore, VIS-NIR is relevant for studies on bodies where pristine rocks have been altered by, but not exclusively, acid and/or aqueous processes, such as Mars. Hydrated silica include a diverse group of silica-rich

materials such as chert, opal, quartz, and natural sinters (Rice et al., 2013) whose existence has been found to depend on the specific environmental conditions and formation processes (Rice et al., 2013). The identification of siliceous sinter as the specific type of hydrated silica in our study area corresponds to the anticipated material that could have been formed when H_2S emissions from fumaroles oxidize and condense to form solutions with a low pH (<2). These solutions react with volcanic deposits and lead to the formation of secondary minerals, that is, salts, leaving silica behind as the major residual (Rice et al., 2013) and keeping the structures and textures of the pristine rock as observed in the study area. This Si-rich residue can also be described as amorphous silica (Pisello et al., 2023) that is morphologically similar to silica sinter. Siliceous sinter often contains sulfates like jarosite and alunite as observed on Vulcano, but also kaolinite and anatase (TiO_2) and additional components (Rodgers et al., 2002; Ruff et al., 2011; White et al., 1988).

In summary, the identified mineral assemblage is believed to be a direct result of the interaction between the surface of the lava deposits and volcanically-derived acid fluids. Acid gases (SO_2, HCl, HF), which are believed to mainly originate from the magmatic reservoir of the La Fossa volcano at a depth between 2 and 3 km (Bolognesi & D'Amore, 1993; Chiodini et al., 1995; Capasso et al., 1997; Gioncada et al., 1998), emanate from vents and cracks and react with fluids such as rain or seawater to form sulfuric acid (Fulignati et al., 1998, 2002; Fulignati & Sbrana, 1998) which then interacts with the surface of the lava rock. Compounds of the minerals in the lava rock can become dissolved and are used to form new secondary minerals.

Thus, our study confirms that the original lava rock is more or less completely leached, leaving behind altered rocks with a content of more than 90wt% of SiO_2 (Fulignati et al., 1998, 2002). This also explains why no clays such as kaolinite could be identified in the study area. Kaolinite could only occur if the formation of hydrated silica is at least partly prevented (Iler, 1955), and silica, precipitating from supersaturated solutions can react with cations such as Al^{3+} to form silicates. In the study area, however, the remobilized material is consumed by the formation of the secondary mineral phases jarosite and alunite (argillic alteration). Similarly, the breakdown of the primary minerals of the lava rock also results in the liberation of calcium next to silica, which is used to form gypsum (Vishiti et al., 2018).

The majority of the observed minerals only form and remain stable in a limited range of environmental conditions (Cloutis et al., 2006; Cull-Hearth et al., 2016) and can be used as possible indicators to constrain the specific environmental conditions, such as the range of pH values and temperature, as well as the available cations and anions of past aqueous environments. Thus, minerals, such as those identified on Vulcano, are useful markers for understanding the geologic and climatic evolution of Mars and other planetary bodies. Particularly, the ability to distinguish between different sulfate minerals, as in the study area, can help in understanding the geological and climatic evolution of sulfate-bearing targets (e.g., Buckby et al., 2003; Jerz & Rimstidt, 2003; Murad & Rojík, 2003; Vaniman et al., 2004). Indeed, several theories have been proposed for the aqueous formation of sulfates on the surface of Mars (Hurowitz et al., 2010; Ming et al., 2008; Nachon et al., 2014; Rapin et al., 2019; Vaniman et al., 2024) with acid alteration of lava rocks by SO_2-bearing volcanic gases—similar to what can be seen on Vulcano—being one of the favored scenarios (Squyres et al., 2007).

In addition, hydrated silica have also been identified in various locations on Mars, both from orbital and in-situ-data, in different geological settings (Beck et al., 2025; Pan et al., 2014; Pineau et al., 2020; Rice et al., 2013; Sun & Milliken, 2018; Tarnas et al., 2019). As on Earth, its degree of hydration and crystallization has been found to be an important indicator of past aqueous conditions. For instance, opal may be associated with Martian bedrock, while more crystalline silica are often linked to aeolian but unconsolidated deposits (Sun & Milliken, 2018). Therefore, studying hydrated silica on Earth—particularly its degree of hydration and crystallization in the geologic context—can help to elucidate its formation processes on Mars, whether through (a) primary precipitation from solution, (b) diagenetic alteration, or (c) replacement of minerals (Pineau et al., 2020; Rice et al., 2013).

7. Conclusions—Potential of a Multi-Instrument Concept for Future Field and Planetary Exploration

The combination of the VIS-NIR results with LIBS and Raman measurements for our field research significantly improved the characterization of the spectral properties of the volcanic deposits in the study area, providing a more comprehensive view into their alteration processes. Identifying the complete assemblage of minerals present within an outcrop is crucial for reconstructing the aqueous history of the study area (Cull-Hearth et al., 2016) and

for applying this knowledge to study similar alteration processes on Mars. Therefore, potentially spectrally masked or subdued minerals must be considered when interpreting environmental conditions using VIS-NIR spectral analyses in the field—both in terrestrial fieldwork and especially, in planetary exploration using remote-sensing techniques (Flahaut et al., 2017).

Studying the advantages and limitations of each instrument in relation to the different geological and mineralogical context of specific target areas provides valuable insight for future field studies, scientific objectives, and mission planning. This also applies to the application of each instrument and its spectral techniques in upcoming planetary missions. Analyzing planetary analog environments such as Vulcano offers a valuable tool for improving our understanding of the mineralogical and geochemical processes associated with acid alteration of lava rocks. These insights can directly support the scientific work in the frame of the ongoing NASA-led Mars2020 and ESA's planned ExoMars mission (Gardini et al., 2006), where a combination of spectral instruments similar to those presented in this study are involved.

The potential of the three instruments is expected to vary depending on the specific geological environments and the scientific questions in the field of planetary exploration. Continued research into how best to integrate different in-situ spectral instruments with orbital data, under different geologic environment (Stephan et al., 2024) will further refine our ability to better characterize diverse planetary surfaces.

Data Availability Statement

All the data used in this work can be found in a repository following the FAIR principles (Stephan, Rammelkamp, Baqué, Schröder et al., 2024).

Acknowledgments
The Vulcano Summer School in 2019 was an extension of the successful previous four Summer Schools, which were supported by the Helmholtz Alliance Robotic Exploration of Extreme Environments (ROBEX) and then supported by EU-Europlanet program. The Vulcano Summer School 2022 is supported by the ARCHES Project (Helmholtz Association Project Alliance ZT-0033) with institutional support from various universities and research institutions such as the German Aerospace Center (DLR), the German Research Centre for Artificial Intelligence (DFKI), the University of Perugia, Constructor University Bremen (CU) and Freiberg University of Mining and Technology (TUBAF). Open Access funding enabled and organized by Projekt DEAL.

References

Abdel-Harith, M., & Abdel-Salam, Z. (2022). Principal component analysis. In V. Palleschi. (Ed.). *Chemometrics and numerical methods in LIBS*. https://doi.org/10.1002/9781119759614.ch5

Aiuppa, A., Bitetto, M., Calabrese, S., Delle Donne, D., Lages, J., La Monica, F. P., et al. (2022). Mafic magma feeds degassing unrest at Vulcano Island, Italy. *Communications Earth & Environment*, *3*(1), 255. https://doi.org/10.1038/s43247-022-00589-1

Anbalagan, G., Mukundakumari, S., Murugesan, K. S., & Gunasekaran, S. (2008). Infrared, optical absorption, and EPR spectroscopic studies on natural gypsum. *Vibrational Spectroscopy*, *50*(2), 226–230. https://doi.org/10.1016/j.vibspec.2008.12.004

Arrighi, S., Tanguy, J. C., & Rosi, M. (2006). Eruptions of the last 2200 years at Vulcano and Vulcanello (Aeolian Islands, Italy) dated by high-accuracy archeomagnetism. *Physics of the Earth and Planetary Interiors*, *159*(3–4), 225–233. https://doi.org/10.1016/j.pepi.2006.07.010

Barberi, F., Neri, G., Valenza, M., & Villari, L. (1991). 1987 – 1990 unrest at Vulcano. *Acta Vulcanologica*, *1*, 95–106.

Beck, P., Beyssac, O., Dehouck, E., Bernard, S., Oneau, M., Mandon, L., et al. (2025). From hydrated silica to quartz: Potential hydothermal precipitates found in Jezero Crater, Mars. *Earth and Planetary Science Letters*, *656*, 119256. https://doi.org/10.1016/j.epsl.2025.119256

Beegle, L., Bhartia, R., White, M., DeFlores, L., Abbey, W., Wu, Y.-H., et al. (2015). SHERLOC: Scanning habitable environments with Raman luminescence for organics chemicals. In *2015 IEEE Aerospace conference*.

Belousova, E. A., Griffin, W. L., O'Reilly, S. Y., & Fisher, N. I. (2002). Apatite as an indicator mineral for mineral exploration: Trace-element compositions and their relationship to host rock type. *Journal of Geochemical Exploration*, *76*(1), 45–69. https://doi.org/10.1016/s0375-6742(02)00204-2

Bishop, J. L., & Murad, E. (2005). The visible and infrared spectral properties of Jarosite and Alunite. *American Mineralogist*, *90*, 1100–1107.

Bolognesi, L., & D'Amore, F. (1993). Isotopic variation of the hydrothermal system on Vulcano Island, Italy. *Geochim. Cosmochim.*, *57*(9), 2069–2082. https://doi.org/10.1016/0016-7037(93)90094-d

Böttger, U., de Vera, J.-P., Hermelink, A., Fritz, J., Weber, I., Schulze-Makuch, D., & Hübers, H.-W. (2013). Application of Raman spectroscopy as in situ technology for the search for life. In J.-P. de Vera & J. Seckbach (Eds.), *Habitability of other planets and satellites*. Springer. https://doi.org/10.1007/978-94-007-6546-7_18

Buckby, T., Black, S., Coleman, M. L., & Hodson, M. E. (2003). Fe-sulfate-rich evaporative mineral precipitates from the Rio Tinto, Southwest Spain. *Mineralien Magazine*, *67*(2), 263–278. https://doi.org/10.1180/0026461036720104

Capasso, G., Favara, R., & Inguaggiato, S. (1997). Chemical features and isotopic composition of gaseous manifestations on Vulcano Island, Aeolian Islands, Italy: An interpretative model of fluid circulation. *Geochimica et Cosmochimica Acta*, *61*(16), 3425–3440. https://doi.org/10.1016/s0016-7037(97)00163-4

Chen, Y. H., Huang, E., Yu, S. C., & Lee, P. L. (2010). Raman spectroscopy and X-ray diffraction studies on celestite. *Physica B: Condensed Matter*, *405*(20), 4386–4388. https://doi.org/10.1016/j.physb.2010.08.001

Chiodini, G., Cioni, R., Marini, L., & Panichi, C. (1995). Origin of the fumarolic fluids of Vulcano Island, Italy and implications for volcanic surveillance. *Bulletin of Volcanology*, *57*(2), 99–110. https://doi.org/10.1007/bf00301400

Cho, Y., Böttger, U., Rull, F., Hübers, H.-W., Belenguer, T., Börner, A., et al. (2021). In situ science on Phobos with the Raman spectrometer for MMX (RAX): Preliminary design and feasibility of Raman measurements. *Earth Planets and Space*, *73*(1), 232. https://doi.org/10.1186/s40623-021-01496-z

Clark, R. N., Swayze, G. A., Gallagher, A., Gorelick, N., & Kruse, F. (1991). Mapping with imaging spectrometer data using the complete band shape least-squares algorithm simultaneously fit to multiple spectral features from multiple materials. In *Proceedings of the third Airborne visible/Infrared Imaging Spectrometer (AVIRIS) workshop* (Vol. 42, pp. 2–3). La Cañada Flintridge, CA, USA: Jet Propulsion Laboratory.

Cloutis, E. A., Hawthorne, F. C., Mertzman, S. A., Krenn, K., Craig, M. A., Marcino, D., et al. (2006). Detection and discrimination of sulfate minerals using reflectance spectroscopy. *Icarus*, *184*(1), 121–157. https://doi.org/10.1016/j.icarus.2006.04.003

Connors, B., Somers, A., & Day, D. (2016). Application of handheld Laser-Induced Breakdown Spectroscopy (LIBS) to geochemical analysis. *Applied Spectroscopy*, *70*(5), 810–815. https://doi.org/10.1177/0003702816638247

Cull-Hearth, S., van Venrooy, A., Clark, M. C., & Cvitkovic, A. (2016). Acid-sulfate mixtures from Río Tinto, Spain: Spectral masking relationships and implications for Mars. *Icarus*, *271*, 387–399.

Dallara, E., Fulignati, P., Costa, S., Gioncada, A., Langone, A., & Pistolesi, M. (2023). Apatite chemistry in shoshonitic magmas: Insights into the volatile evolution at La Fossa volcano (Vulcano Island, Aeolian Arc, Italy). *Lithos*, *454 – 455*, 107238. https://doi.org/10.1016/j.lithos.2023.107238

De Astis, G., Dellino, P., La Volpe, L., Lucchi, F., & Tranne, C. A. (2006). *Geological map of the Vulcano Island (1:10,000)*. Litografia artistica cartografica.

De Astis, G., La Volpe, L., Peccerillo, A., & Civetta, L. (1997). Volcanological and petrological evolution of Vulcano Island (Aeolian Arc, Southern Tyrrenian Sea). *Journal of Geophysical Research*, *102*(B4), 8021–8050. https://doi.org/10.1029/96jb03735

De Astis, G., Lucchi, F., Dellino, P., La Volpe, L., Tranne, C. A., Frezzotti, M. L., & Peccerillo, A. (2013). Geology, volcanic history and petrology of Vulcano (Central Aeolian Archipelago). *Geological Society of London*, *37*(1), 281–349. https://doi.org/10.1144/m37.11

De Astis, G., Peccerillo, A., Kempton, P. D., La Volpe, L., & Wu, T. W. (2000). Transition from calc-alkaline to potassium-rich magmatism in subduction environments: Geochemical and Sr, Nd, Pb isotopic constraints from the Island of Vulcano (Aeolian Arc). *Contributions to Mineralogy and Petrology*, *139*(6), 684–703. https://doi.org/10.1007/s004100000172

Di Traglia, F., Pistolesi, M., Rosi, M., Bonadonna, C., Fusillo, R., & Roverato, M. (2013). Growth and erosion: The volcanic geology and morphological evolution of La Fossa (Island of Vulcano, Southern Italy) in the last 1000 years. *Geomorphology*, *194*, 94–107. https://doi.org/10.1016/j.geomorph.2013.04.018

Edwards, H. G. M., Hassan, N. F. N., & Middleton, P. S., (2006). Anatase - A pigment in ancient artwork or a modern usurper? *Analytical and Bioanalytical Chemistry*, *384*, 1356–1365.

Ehlmann, B. L., Mustard, J. F., Swayze, G. A., Clark, R. N., Bishop, J. L., Poulet, F., et al. (2009). Identification of hydrated silicate minerals on Mars using MRO-CRISM: Geologic context near Nili Fossae and implications for aqueous alteration. *J. Geophys. Res.Planets*, *114*(E2), 1–33. https://doi.org/10.1029/2009JE003339

El Haddad, J., Canioni, L., & Bousquet, B. (2014). Good practices in LIBS analysis: Review and advices. *Spectrochimica Acta Part B: Atomic Spectroscopy*, *101*, 171–182. https://doi.org/10.1016/j.sab.2014.08.039

Ellery, A., & Wynn-Williams, D. (2003). Why Raman spectroscopy on Mars? A case of the right tool for the right job. *Astrobiology*, *3*, 565–579. https://doi.org/10.1089/153110703322610654

Fabre, C., Ourti, N. E., Mercadier, J., Cardoso-Fernandes, J., Dias, F., Perrotta, M., et al. (2021). Analyses of Li-rich minerals using handheld LIBS tool. *Data*, *6*(6), 68. https://doi.org/10.3390/data6060068

Flahaut, J., Martinot, M., Bishop, J. L., Davies, G. R., & Potts, N. (2017). Remote sensing and in situ mineralogic survey of the Chilean salars: An analog to Mars evaporate deposits. *Icarus*, *282*, 152–173. https://doi.org/10.1016/j.icarus.2016.09.041

Flörke, O. W., Graetsch, H., Martin, B., Röller, K., & Wirth, R. (1991). Nomenclature of micro- and non-crystalline silica minerals, based on structure and microstructure. *Neues Jahrbuch für Mineralogie*, *163*(1), 19–42.

Forjanes, P., Astilleros, J. M., & Fernández-Díaz, L. (2020). The Formation of barite and celestite through the replacement of gypsum. *Minerals*, *10*(2), 189. https://doi.org/10.3390/min10020189

Foucher, F., Ammar, M.-R., & Westall, F. (2015). Revealing the biotic origin of silicified Precambrian carbonaceous microstructures using Raman spectroscopic mapping, a potential method for the detection of microfossils on Mars. *Journal of Raman Spectroscopy*, *46*(10), 873–879. https://doi.org/10.1002/jrs.4687

Frost, R. L., Wills, R.-A., Martens, W., & Weier, M. (2005). NIR spectroscopy of jarosites. *Spectrochimica Acta Part A: Molecular and Biomolecular Spectroscopy*, *62*(4), 869–874. https://doi.org/10.1016/j.saa.2005.03.018

Frost, R. L., Wills, R.-A., Weier, M. L., Martens, W., & Kloprogge, J. T. (2006). A Raman spectroscopic study of Alunites. *Journal of Molecular Structure*, *785*(1–3), 123–132. https://doi.org/10.1016/j.molstruc.2005.10.003

Fulignati, P., Gioncada, A., & Sbrana, A. (1998). Geologic model of the magmatic-hydrothermal system of Vulcano (Aeolian Island, Italy). *Mineralogy and Petrology*, *62*(3–4), 195–222. https://doi.org/10.1007/bf01178029

Fulignati, P., & Sbrana, A. (1998). Presence of native gold and tellurium in the active high-sul¢dation hydrothermal system of the La Fossa Volcano (Vulcano, Italy). *Journal of Volcanology and Geothermal Research*, *86*(1–4), 187–198. https://doi.org/10.1016/s0377-0273(98)00078-x

Fulignati, P., Sbrana, A., Luperini, W., & Greco, V. (2002). Formation of rock coatings induced by the acid fumarole plume of the passively degassing volcano of La Fossa (Vulcano Island, Italy). *Journal of Volcanology and Geothermal Research*, *115*(3–4), 397–410. https://doi.org/10.1016/s0377-0273(02)00209-3

Fusillo, R., Di Traglia, F., Gioncada, A., Pistolesi, M., Wallace, P. J., & Rosi, M. (2015). Deciphering post-caldera volcanism: Insight into the Vulcanello (Island of Vulcano, Southern Italy) eruptive activity based on geological and petrological constraints. *Bulletin of Volcanology*, *77*(9), 1–23. https://doi.org/10.1007/s00445-015-0963-6

Gardini, B., Vago, J. L., Baglioni, P., Kminek, G., & Gianfiglio, G. (2006). ExoMars: ESA's mission to search for signs of life on the red planet. In *36th COSPAR scientific assembly, 16 - 23 July 2006, Beijing, China. Meeting abstract from the CDROM, #554*.

Georgiev, D., Pedersen, S., Xie, R., Fernández-Galiana, Á., Stevens, M., & Barahona, M. (2023). RamanSPy: An open-source Python package for integrative Raman spectroscopy data analysis. *ChemRxiv*. https://doi.org/10.26434/chemrxiv-2023-m3xlm

Gioncada, A., Clocchiatti, R., Sbrana, A., Bottazzi, P., Massare, D., & Ottolini, L. (1998). A study of melt inclusions at Vulcano (Aeolian Islands, Italy): Insight on the primitive magmas and on the volcanic feeding system. *Bulletin Volcanologique*, *60*(4), 286–306. https://doi.org/10.1007/s004450050233

Graetsch, H. (1994). Structural characteristics of opaline and microcrystalline silica minerals. *Reviews in Mineralogy and Geochemistry*, *29*(1), 209–232.

Hermann, J., Gerhard, C., Axente, E., & Dutouquet, C. (2014). Comparative investigation of laser ablation plumes in air and argon by analysis of spectral line shapes: Insights on calibration-free laser-induced breakdown spectroscopy. *Spectrochimica Acta Part B: Atomic Spectroscopy*, *100*, 189–196. https://doi.org/10.1016/j.sab.2014.08.014

Hope, G. A., Woods, R., & Munce, C. G. (2001). Raman microprobe mineral identification. *Minerals Engineering*, *14*(12), 1565–1577. https://doi.org/10.1016/s0892-6875(01)00175-3

Hunt, G. R. (1977). Spectral signatures of particulate minerals in the visible and near-infrared. *Geophysics*, *42*(3), 501–513. https://doi.org/10.1190/1.1440721

Hunt, G. R., Salisbury, J. W., & Lenhoff, C. J. (1971). Visible and near-infrared spectra of minerals and rocks: IV. Sulphides and sulphates. *Modern Geology*, *3*, 1–14.

Hurowitz, J. A., Fischer, W. W., Tosca, N. J., & Milliken, R. E. (2010). Origin of acidic surface waters and the evolution of atmospheric chemistry on early Mars. *Nature Geoscience*, *3*(5), 323–326. https://doi.org/10.1038/ngeo831

Ikehata, K., Arakawa, Y., & Ishibashi, J. (2021). Raman microspectroscopic study of reference clay minerals and alteration minerals in volcanic ejecta from the 7 March 2012 phreatic eruption on Ioto Island (Iwo-Jima), Izu-Bonin arc, Japan. *Vibrational Spectroscopy*, *114*, 103247. https://doi.org/10.1016/j.vibspec.2021.103247

Iler, R. K. (1955). *The colloid chemistry of silica and silicates*. Cornell University Press. 1955. xii + 324.

Jerz, J. K., & Rimstidt, J. D. (2003). Efflorescent iron sulfate minerals: Paragenesis, relative stability, and environmental impact. *American Mineralogist*, *88*(11–12), 1919–1932. https://doi.org/10.2138/am-2003-11-1235

Kokaly, R. F., Clark, R. N., Swayze, G. A., Livo, K. E., Hoefen, T. M., Pearson, N. C., et al. (2017). *USGS spectral library version 7* (Vol. 1035, p. 61). U.S. Geological Survey Data Series. https://doi.org/10.3133/ds1035

Kramida, A., Ralchenko, Y., & Reader, J., & NIST ASD Team. (2023). *NIST atomic spectra database (version 5.11)*. National Institute of Standards and Technology. https://doi.org/10.18434/T4W30F

Kruse, F. A., Lefkoff, A. B., Boardman, J. B., Heidebreicht, K. B., Shapiro, A. T., Barloon, P. J., & Goetz, A. F. H. (1993). The Spectral Image Processing System (SIPS)—Interactive visualization and analysis of imaging spectrometer data. *Remote Sensing of Environment*, *44*(2–3), 145–163. https://doi.org/10.1016/0034-4257(93)90013-n

Lafuente, B., Downs, R. T., Yang, H., & Stone, N. (2016). The power of databases: The RRUFF project. In T. Armbruster & R. M. Danisi (Eds.), *Highlights in mineralogical crystallography* (pp. 1–30). Walter de Gruyter GmbH. https://doi.org/10.1515/9783110417104-003

Le Maitre, R. W. (2002). *Igneous rocks — a classification and glossary of terms* (2nd ed., p. 141). Cambridge University Press.

Ling, Z. C., Cao, F. K., Ni, Y. H., Wu, Z. C., Zhang, J., & Li, B. (2015). Raman spectroscopic studies of K-Na jarosite solid solutions. In *46th LPSC, # 2598*.

Liu, C., Ling, Z., Zhang, J., Bi, X., & Xin, Y. (2020). Laboratory Raman and VNIR spectroscopic studies of jarosite and other secondary mineral mixtures relevant to Mars. *Journal of Raman Spectroscopy*, *51*(9), 1575–1588. https://doi.org/10.1002/jrs.5809

Liu, Y., Wang, A., & Freeman, J. J. (2009). Raman, Mir, and NIR spectroscopic study of calcium sulfates; gypum. *LPI Contributions, 40th LPSC*, 2128.

Mabrouk, K. B., Kauffmann, T. H., Aroui, H., & Fontana, M. D. (2013). Raman study of cation effect on sulfate vibration modes in solid state and in aqueous solutions. *Journal of Raman Spectrsocopy*, *44*(11), 1603–1608. https://doi.org/10.1002/jrs.4374

Malaguti, A. B., Rosi, M., Pistolesi, M., Speranza, F., & Menzies, M. (2022). The contribution of palaeomagnetism, tephrochronology and radiocarbon dating to refine the last 1100 years of eruptive activity at Vulcano (Italy). *Bulletin of Volcanology*, *84*(1), 1–19. https://doi.org/10.1007/s00445-021-01515-7

Mandarano, M., Paonita, A., Martelli, M., Viccaro, M., Nicotra, E., & Millar, I. L. (2016). Revealing magma degassing below closed-conduit active volcanoes: Geochemical features of volcanic rocks versus fumarolic fluids at Vulcano (Aeolian Islands, Italy). *Lithos*, *248*, 272–287. https://doi.org/10.1016/j.lithos.2016.01.026

Marcaida, I., Maguregui, M., Morillas, H., Veneranda, M., Prieto-Taboada, N., Fdez-Ortiz de Vallejuelo, S., & Madariaga, J. M. (2019). Raman microscopy as a tool to discriminate mineral phases of volcanic origin and contaminations on red and yellow ochre raw pigments from Pompeii. *Journal of Raman Spectroscopy*, *50*(2), 143–149. https://doi.org/10.1002/jrs.5414

Maubec, N., Lahfid, A., Lerouge, C., Wille, G., & Michel, K. (2012). Characterization of alunite supergroup minerals by Raman spectroscopy. *Spectrochimica Acta Part A: Molecular and Biomolecular Spectroscopy*, *96*, 925–939. https://doi.org/10.1016/j.saa.2012.07.094

Maurice, S., Wiens, R. C., Bernardi, P., Caïs, P., Robinson, S., Nelson, T., et al. (2021). The SuperCam instrument suite on the Mars 2020 rover: Science objectives and mast-unit description. *Space Science Reviews*, *217*(3), 47. https://doi.org/10.1007/s11214-021-00807-w

Ming, D. W., Morris, R. V., Benton, C. C., & Lockheed, M. (2008). Chapter 23: Aqueous alteration on Mars. In J. F. Bell III (Ed.), *The Martian surface: Composition, mineralogy, and physical properties* (pp. 519–540). Cambridge University Press.

Murad, E. (1997). Identification of minor amounts of Anatase in Kaolins by Raman spectroscopy. *American Mineralogist*, *82*(1–2), 203–206. https://doi.org/10.2138/am-1997-1-222

Murad, E., & Rojík, P. (2003). Iron-rich precipitates in a mine drainage environment: Influence of pH on mineralogy. *American Mineralogist*, *88*, 1915–1918.

Murchie, S., Arvidson, R., Deini, P., Beisser, K., Bibring, J.-B., Bishop, J., et al. (2007). Compact Reconnaissance Imaging Spectrometer for Mars (CRISM) on Mars Reconnaissance Orbiter (MRO). *Journal of Geophysical Research*, *112*(E5), E05S03. https://doi.org/10.1029/2006JE002682

Murphy, P. J., Smith, A., Hudson-Edwards, M. L., Dubbin, K. A., William, E., & Wright, K. (2009). Raman and IR spectroscopic studies of alunite-supergroup compounds containing Al, Cr^{3+}, Fe^{3+} and V^{3+} at the B site. *The Canadian Mineralogist*, *47*(3), 663–681. https://doi.org/10.3749/canmin.47.3.663

Nachon, M. C., Mangold, S. M., Schröder, N., Kah, S., Dromart, L. C., Ollila, G., et al. (2014). Calcium sulfate veins characterized by ChemCam/Curiosity at Gale crater, Mars. *JGR Planets*, *119*(9), 1991–2016. https://doi.org/10.1002/2013je004588

Němečková, K., Jehlička, J., & Culka, A. (2020). Fast screening of carotenoids of gypsum endoliths using portable Raman spectrometer (Messinian gypsum, Sicily). *Journal of Raman Spectroscopy*, *51*(7), 1127–1137. https://doi.org/10.1002/jrs.5891

Nicotra, E., Giuffrida, M., Viccaro, M., Donato, P., D'Oriano, C., Paonita, A., & De Rosa, R. (2018). Timescales of pre-eruptive magmatic processes at Vulcano (Aeolian Islands, Italy) during the last 1000 years. *Lithos*, *316–317*, 347–365. https://doi.org/10.1016/j.lithos.2018.07.028

Pan, L., & Ehlmann, B. L. (2014). Phyllosilicate and hydrated silica detections in the knobby terrains of Acidalia Planitia, Northern Plains, Mars. *Geophysical Research Letters*, *41*(6), 1890–1898. https://doi.org/10.1002/2014GL059423

Peccerillo, A. (2005). *Plio-quaternary volcanism in Itali* (p. 365). Springer. https://doi.org/10.1007/3-540-29092-3

Pineau, M., Le Deit, L., Chauviré, B., Carter, J., Rondeau, B., & Mangold, N. (2020). Toward the geological significance of hydrated silica detected by near infrared spectroscopy on Mars based on terrestrial reference samples. *Icarus*, *347*, 113706. https://doi.org/10.1016/j.icarus.2020.113706

Pisello, A., Bisolfati, M., Poggiali, G., Tolomei, P., Braschi, E., Brucato, J. R., & Perugini, D. (2023). Mid-infrared (MIR) spectroscopy of silicate glasses as analogs for mercury's surface: The influence of grain size. *Minerals*, *13*(2), 170. https://doi.org/10.3390/MIN13020170

Pisello, A., De Angelis, S., Ferrari, M., Porreca, M., Vetere, F. P., Behrens, H., et al. (2022). Visible and Near-InfraRed (VNIR) reflectance of silicate glasses: Characterization of a featureless spectrum and implications for planetary geology. *Icarus*, *374*, 114801. https://doi.org/10.1016/j.icarus.2021.114801

Qiu, J., Li, X., & Qi, X. (2019). Raman spectroscopic investigation of sulfates using mosaic grating spatial heterodyne Raman spectrometer. *IEEE Photonics Journal*, *11*(5), 1–12. https://doi.org/10.1109/JPHOT.2019.2939222

Rammelkamp, K., Schröder, S., Ortenzi, G., Pisello, A., Stephan, K., Baqué, M., et al. (2021). Field investigation of volcanic deposits on Vulcano, Italy using a handheld laser-induced breakdown spectroscopy instrument. *Spectrochimica Acta Part B: Atomic Spectroscopy*, *177*, 106067. https://doi.org/10.1016/j.sab.2021.106067

Rammelkamp, K., Schröder, S., Pisello, A., Ortenzi, G., Sohl, F., & Unnithan, V. (2023). Explorative data analysis methods: Application to laser-induced breakdown spectroscopy field data measured on the Island of Vulcano, Italy. *Sensors*, *23*(13), 6208. https://doi.org/10.3390/s23136208

Rapin, W., Ehlmann, B. L., Dromart, G., Schieber, J., Thomas, N. H., Fischer, W. W., et al. (2019). An interval of high salinity in ancient Gale crater lake on Mars. *Nature Geoscience*, *12*(11), 889–895. https://doi.org/10.1038/s41561-019-0458-8

Rice, M. S., Cloutis, E. A., Bell III, J. F., Bish, D. L., Horgan, B. H., Mertzman, S. A., et al. (2013). Reflectance spectra diversity of silica-rich materials: Sensitivity to environment and implications for detections on Mars. *Icarus*, *223*(1), 499–533. https://doi.org/10.1016/j.icarus.2012.09.021

Rodgers, K. A., Cook, K. L., Browne, P. R. L., & Campbell, K. A. (2002). The mineralogy, texture and significance of silica derived from alteration by steam condensate in three New Zealand geothermal fields. *Clay Minerals*, *37*(2), 299–322. https://doi.org/10.1180/0009855023720035

Ruff, S. W., Farmer, J. D., Wendy, W. M., Herkenhoff, K. E., Johnson, J. R., Morris, R. V., et al. (2011). Characteristics, distribution, origin, and significance of opaline silica observed by the Spirit rover in Gusev crater, Mars. *Journal of Geophysical Research*, *116*, E00F23. https://doi.org/10.1029/2010JE003767

Rull, F., Maurice, S., Hutchinson, I., Moral, A., Perez, C., Diaz, C., & the RLS Team. (2017). The Raman laser spectrometer for the ExoMars rover mission to Mars. *Astrobiology*, *17*(6–7), 627–654. https://doi.org/10.1089/ast.2016.1567

Schröder, S., Böttger, U., Buder, M., Bunduki, Y., Cho, Y., Dietz, E., et al. (2023). RAX: The Raman spectrometer on the MMX rover for in-situ surface analysis on Phobos. In *54th LPSC* (Vol. 2806, 2549). LPI Contribution.

Schröder, S., Rammelkamp, K., Hanke, F., Weber, I., Vogt, D. S., Frohmann, S., et al. (2020). Effects of pulsed laser and plasma interaction on Fe, Ni, Ti, and their oxides for LIBS Raman analysis in extraterrestrial environments. *Journal of Raman Spectroscopy*, *51*(9), 1667–1681. https://doi.org/10.1002/jrs.5650

Senesi, G. S., Harmon, R. S., & Hark, R. R. (2021). Field-portable and handheld laser-induced breakdown spectroscopy: Historical review, current status and future prospects. *Spectrochimica Acta Part B: Atomic Spectroscopy*, *175*(October 2020), 106013. https://doi.org/10.1016/j.sab.2020.106013

Sirven, J.-B., Bousquet, B., Canioni, L., & Sarger, L. (2006). Laser-induced breakdown spectroscopy of composite samples: Comparison of advanced chemometrics methods. *Analytical Chemistry*, *78*(5), 1462–1469. https://doi.org/10.1021/ac051721p

Squyres, S. W., Aharonson, O., Clark, B. C., Cohen, B. A., Crumpler, L., de Souza, P. A., et al. (2007). Pyroclastic activity at home plate in Gusev Crater, Mars. *Science*, *316*(5825), 738–742. https://doi.org/10.1126/science.1139045

Stephan, K., Hauber, E., Franchi, F., Rammelkamp, K., Baque, M., Schröder, S., & Motlhasedi, A. (2024). Spectral field study of the Makgadikgadi Salt Pans in Botswana as a planetary analog for ancient fluvio-lacustrine environments on Mars. *EPSC Abstracts*, *18*, EPSC2024743.

Stephan, K., Rammelkamp, K., Baqué, M., Schröder, S., Pisello, A., Gwinner, K., et al. (2024). Dataset: Multi-Spectral field study of planetary analog material in extreme environments – Alteration products of volcanic deposits of Vulcano/Italy [Dataset]. *Zenodo*. https://doi.org/10.5281/zenodo.13960797

Stephan, K., Schröder, S., Rammelkamp, K., Gwinner, K., Haber, J., Varatharajan, I., et al. (2020). Multi-spectral investigation of planetary analog material in extreme environments - alteration products of volcanic deposits of Vulcano/Italy. *EPSC Abstracts*, *13*, 20192411. EPSC-DPS2019-2062.

Sun, V. Z., & Milliken, R. E. (2018). Distinct geologic settings of opal-A and more crystalline hydrated silica on Mars. *Geophysical Research Letters*, *45*(19), 10–221. https://doi.org/10.1029/2018GL078494

Tarnas, J. D., Mustard, J. F., Lin, H., Goudge, T. A., Amador, E. S., Bramble, M. S., et al. (2019). Orbital identification of hydrated silica in Jezero crater, Mars. *Geophysical Research Letters*, *46*(22), 12–771. https://doi.org/10.1029/2019GL085584

Tranne, C. A., Lucchi, F., Calanchi, N., Lanzafame, G., & Rossi, P. L. (2002). Geological map of the island of Lipari (Aeolian Islands). *Università di Bologna*.

Unnithan, V., Thomsen, L., Sohl, F., Baqué, M., Gwinner, K., Haber, J., et al. (2019). Vulcano summer School 2019: Field-based terrestrial, marine and planetary analogue studies. In: EPSC-DPS joint meeting 2019. *EPSC Abstracts*, *13*, 2051.

Vaniman, D., Chipera, S., Rampe, E., Bristow, T., Blake, D., Meusburger, J., et al. (2024). Gypsum on Mars: A detailed view at gale crater. *Minerals*, *14*(8), 815. https://doi.org/10.3390/min14080815

Vaniman, D. T., Bish, D. L., Chipera, S. J., Flalips, C. I., Carey, J. W., & Feldman, W. C. (2004). Magnesium sulphate salts and the history of water on Mars. *Nature*, *431*(7009), 663–665. https://doi.org/10.1038/nature02973

Vishiti, A., Armstrong, T., Shemang, E. M., Etame, J., & Suh, C. E. (2018). Hydrothermal alteration of basaltic rocks at eruptive vents on mount Cameroon Volcano, West Africa. *International Journal of Geosciences*, *9*(9), 513–527. https://doi.org/10.4236/ijg.2018.99030

Viviano-Beck, C. E. (2015). *MRO CRISM type spectra library*. NASA Planetary Data System. Retrieved from https://crismtypespectra.rsl.wustl.edu

Vogt, D. S., Schröder, S., Rammelkamp, K., Hansen, P. B., Kubitza, S., & Hübers, H.-W. (2020). CaCl and CaF emission in LIBS under simulated Martian conditions. *Icarus*, *335*, 113393. https://doi.org/10.1016/j.icarus.2019.113393

Voltaggio, M., Branca, M., Tuccimei, P., & Tecce, F. (1995). Leaching procedure used in dating young potassic volcanic rocks by the $^{226}Ra/^{230}Th$ method. *EPSL*, *136*(3–4), 123–131. https://doi.org/10.1016/0012-821x(95)00177-e

White, D. E., Hutchinson, R. A., & Keith, T. E. C. (1988). The geology and remarkable thermal activity of Norris geyser basin. *Yellowstone National Park, Wyoming. USGS Professional Paper No. 1456. thermal fluids from mid-ocean ridges* (Vol. 58, 5105–5113). Geochim. Cosmochim. Acta.

Wiens, R. C., Maurice, S., Robinson, S. H., Nelson, A. E., Cais, P., Bernardi, P., et al. (2021). The SuperCam instrument suite on the NASA Mars 2020 rover: Body unit and combined system tests. *Space Science Reviews*, *217*(1), 4. https://doi.org/10.1007/s11214-020-00777-5

Wise, M. A., Harmon, R. S., Curry, A., Jennings, M., Grimac, Z., & Khashchevskaya, D. (2022). Handheld LIBS for Li exploration: An example from the Carolina tin-spodumene Belt, USA. *Minerals*, *12*(1), 77. https://doi.org/10.3390/min12010077

Zhukova, I. A., Stepanov, A. S., Korsakov, A. V., & Jiang, S. (2022). Application of Raman spectroscopy for the identification of phosphate minerals from REE supergene deposit. *Journal of Raman Spectroscopy*, *53*(3), 485–496. https://doi.org/10.1002/jrs.6213